PLANE-WAVE THEORY OF SINGLE-CRYSTAL UPCONVERSION OPTICAL PARAMETRIC OSCILLATORS

A THESIS
SUBMITTED TO THE DEPARTMENT OF ELECTRICAL AND
ELECTRONICS ENGINEERING
AND THE INSTITUTE OF ENGINEERING AND SCIENCES
OF BILKENT UNIVERSITY
IN PARTIAL FULFILLMENT OF THE REQUIREMENTS
FOR THE DEGREE OF
MASTER OF SCIENCE

By
Yamaç Dikmelik
August 1998

PLANE-WAVE THEORY OF SINGLE-CRYSTAL UPCONVERSION OPTICAL PARAMETRIC OSCILLATORS

A THESIS

SUBMITTED TO THE DEPARTMENT OF ELECTRICAL AND

ELECTRONICS ENGINEERING

AND THE INSTITUTE OF ENGINEERING AND SCIENCES

OF BILKENT UNIVERSITY

IN PARTIAL FULFILLMENT OF THE REQUIREMENTS

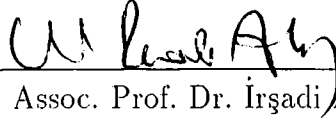FOR THE DEGREE OF

MASTER OF SCIENCE

By

Yamaç Dikmelik

August 1998

I certify that I have read this thesis and that in my opinion it is fully adequate, in scope and in quality, as a thesis for the degree of Master of Science.
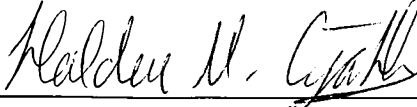
Assoc. Prof. Dr. Orhan Aytür (Supervisor)

I certify that I have read this thesis and that in my opinion it is fully adequate, in scope and in quality, as a thesis for the degree of Master of Science.
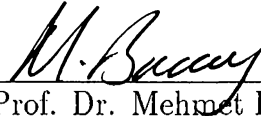
Assoc. Prof. Dr. İrşadi Aksun

I certify that I have read this thesis and that in my opinion it is fully adequate, in scope and in quality, as a thesis for the degree of Master of Science.

Assoc. Prof. Dr. Haldun Özaktaş

Approved for the Institute of Engineering and Sciences:

Prof. Dr. Mehmet Baray
Director of Institute of Engineering and Sciences

ii

ABSTRACT

PLANE-WAVE THEORY OF SINGLE-CRYSTAL UPCONVERSION OPTICAL PARAMETRIC OSCILLATORS

Yamaç Dikmelik

M.S. in Electrical and Electronics Engineering

Supervisor: Assoc. Prof. Dr. Orhan Aytür

August 1998

This thesis presents a theoretical analysis of single-crystal upconversion optical parametric oscillators (OPO's) where a single nonlinear crystal is used for both the OPO and sum-frequency generation (SFG) or second-harmonic generation (SHG). In these devices, the OPO and SFG/SHG processes are both phase matched for the same direction of propagation inside the crystal. Different polarization geometries for which this simultaneous phase matching condition can potentially be satisfied are identified and categorized, for both birefringent and quasi-phase matching methods. This categorization results in four classes of sum-frequency generating OPO's (SF-OPO's) and three classes of self-doubling OPO's (SD-OPO's). Plane-wave coupled mode equations are presented for each of these seven classes. Solutions of these coupled mode equations, and calculation of the single-pass saturated signal gain are outlined. The dependence of the photon conversion efficiency on various design parameters are investigated. A pulsed plane-wave model that takes into account the temporal profiles of the fields and the group velocity mismatch between pulses is constructed. This model is in good qualitative agreement with experimental measurements of a class-C SF-OPO.

Keywords: Nonlinear frequency conversion, optical parametric oscillators, parametric devices, sum-frequency generation, second-harmonic generation. quasi-phase matching

ÖZET

TEK KRİSTALLİ YUKARI-ÇEVRİM OPTİK PARAMETRİK OSİLATÖRLERİNİN DÜZLEM-DALGA TEORİSİ

Yamaç Dikmelik
Elektrik ve Elektronik Mühendisliği Bölümü Yüksek Lisans
Tez Yöneticisi: Doç. Dr. Orhan Aytür
Ağustos 1998

Bu tezde, tek bir doğrusal-olmayan kristalin hem parametrik üretim, hem de toplam-frekansı üretimi (SFG) veya ikinci-harmonik üretimi (SHG) için kullanıldığı tek-kristalli yukarı-dönüşüm optik parametrik osilatörlerinin (OPO) kuramsal analizi sunulmaktadır. Bu cihazlarda, hem OPO hem de SFG/SHG süreçleri kristal içindeki aynı yayılım yönü için faz eşlidir. Bu aynı sırada faz eşli olma koşulunu sağlayabilecek farklı polarizasyon geometrileri, hem çift-kırınımlı hem de yaklaşık faz eşleme yöntemleri için belirlenmiş ve sınıflandırılmıştır. Bunun sonunda, toplam-frekansı üreten OPO'lar (SF-OPO) için dört, ikinci-harmonik üreten OPO'lar (SD-OPO) için üç sınıf belirlenmiştir. Bu yedi sınıf için ayrı ayrı düzlem-dalga bağlı mod denklemleri ve tek-geçişte doygun sinyal kazancı hesabı sunulmuştur. Foton dönüşüm veriminin çeşitli tasarım parametrelerine olan bağlılığı incelenmiştir. Alanların zamansal profilini ve darbe grup hızı uyumsuzluğunu hesaba katan bir darbeli düzlem-dalga modeli oluşturulmuştur. Bu model, deneysel bir C-sınıfı SF-OPO'nun ölçümleri ile uyumlu sonuçlar vermiştir.

Anahtar kelimeler: Doğrusal olmayan frekans dönüşümü, optik parametrik osilatörler, parametrik cihazlar, toplam-frekansı üretimi, ikinci-harmonik üretimi, yaklaşık faz eşleme.

ACKNOWLEDGMENTS

Contents

List of Tables

List of Figures

x

Chapter 1

Introduction

Lasers find applications in many fields such as telecommunications, medicine, defense, printing, entertainment, and basic science. A particular application places various demands on a number of laser properties such as its wavelength, power, beam profile, and bandwidth. One of the most important laser properties is the wavelength of operation.

The operating wavelength of a laser is determined by the energy level differences of the material used as the laser gain medium. For most laser materials, these energy level differences are fixed and the operating wavelength of the laser cannot be tuned. Even though tunable lasers that utilize transitions between broad energy bands exist, the wavelength ranges for these lasers are relatively narrow.

It is of great technological importance to convert the output of a laser to different wavelengths in an efficient manner. This conversion can be achieved using nonlinear optical materials. In such materials, the polarization density has a nonlinear dependence on the electric field. For most nonlinear materials used in frequency conversion, this nonlinear dependence is quadratic. This second-order nonlinear dependence leads to an energy exchange between optical fields at different wavelengths.

Second-order nonlinear interactions lead to such frequency conversion applications as second-harmonic generation (SHG), sum-frequency generation (SFG), and difference-frequency generation (DFG). With SHG, the output beam of a laser can be converted to a beam at twice the frequency. SHG is the most widely used second-order interaction, since this process requires only a single laser. In SFG and DFG, two lasers with different frequencies are used to generate the

sum-frequency or the difference-frequency of the frequencies of the two lasers.

Another second-order interaction is optical parametric amplification; of the two input beams for the DFG process, the lower frequency beam is amplified. The gain provided by an optical parametric amplifier (OPA) can be enclosed in an optical cavity to construct an optical parametric oscillator (OPO), much like a laser amplifier is enclosed in a cavity to construct a laser. The OPO requires a single laser as its input; this laser is the source of energy for the OPO and is said to pump the OPO. The initial light energy at the amplified frequency is provided by parametric fluorescence, similar to spontaneous emission in lasers. This fact also allows for the tunability of OPO's. This tunability is achieved by manipulating the momentum conservation (phase matching) condition by rotating the nonlinear crystal or by changing the crystal's temperature.

By itself, an OPO can only provide downconversion to longer wavelengths. Upconversion to shorter wavelengths is achieved with the use of SHG or SFG in conjunction with an OPO. One approach is to first frequency-double the laser and then use the second-harmonic as the OPO pump [1], [2]. A more widely used technique is to use the OPO output for SHG in a second nonlinear crystal, either outside [3] or inside [4], [5] the OPO cavity. Intracavity SHG is usually more efficient because of the high intensity of the resonant field. SFG of the OPO output with the pump laser also provides upconversion, and can be implemented extracavity or intracavity [6], [7]. These two crystal upconversion OPO's have successfully generated tunable light at visible wavelengths, but with limited conversion efficiencies.

Single-crystal upconversion OPO's, where SHG [8] or SFG [9] takes place within the OPO crystal itself, have recently been demonstrated. These new devices provide highly efficient schemes for frequency upconversion.

The modeling of practical OPO's is an involved task. The simplest approach is to assume that the fields are uniform monochromatic plane waves. However, in a real OPO, the pump beam usually has a Gaussian transverse profile. If the pump laser is pulsed, the temporal profiles of the pulses also have to be taken into account. For OPO's pumped with ultrafast lasers, the ultrashort pulses get separated in the interaction, due to their differing group velocities. This effect is called group velocity mismatch (GVM). Such ultrashort pulses are also broadened in the nonlinear crystal, due to group velocity dispersion (GVD). Furthermore, the intense resonant pulse in the OPO cavity is modified by self-phase modulation,

a third-order nonlinear effect, in the nonlinear crystal. To account for all these effects accurately, coupled nonlinear partial differential equations that govern the propagation and nonlinear interaction of fields have to be solved. Moreover, these solutions should be iterated for several round trips in the OPO cavity, to find the steady-state temporal and transverse profiles of the resonated field.

The plane-wave theory of OPO's was investigated in the early stages of OPO development [10]. The effects of Gaussian profiles were first investigated by assuming plane-wave solutions at each point in the transverse plane [11]. The effects of transverse and temporal profiles for pulsed OPO's operating in the nanosecond regime have recently been investigated with an accurate numerical model [12]. The effects of GVM and GVD on ultrafast OPO performance were first modeled by assuming plane-wave transverse profiles [13], [14], and then by taking into account the more realistic Gaussian profiles [15], [16]. The plane-wave theory for two-crystal upconversion OPO's has also been studied [10], [17], [18]. Even though the plane-wave analyses cannot model an experiment accurately, they bring out the fundamental physics behind these devices.

In this thesis, the plane-wave theory of single-crystal upconversion OPO's is presented. The theoretical background on second-order nonlinear interactions is provided in Chapter 2. Possible phase matching geometries are identified and classified, and the associated sets of differential equations are presented in Chapter 3. Next, solutions of these sets of equations are discussed in Chapter 4. In Chapter 5, the dependence of the conversion efficiency and other OPO performance measures on physical parameters are investigated. A pulsed plane-wave model that takes into account temporal profiles and GVM is constructed in Chapter 6. Finally, conclusions and future directions are presented in Chapter 7.

Chapter 2

Second-Order Nonlinear Interactions

In this chapter, we first present the wave equation for a nonlinear medium, where the polarization density is a nonlinear function of the electric field. Three optical fields interact through a second-order nonlinearity, and this interaction is governed by the coupled mode equations which are presented next. We then discuss phase matching, a condition that has to be satisfied for efficient frequency conversion. We finally introduce optical parametric amplification, optical parametric oscillation, SFG, and SHG.

2.1 The driven wave equation

The interaction of optical fields in a second-order nonlinear medium is governed by the driven wave equation. To arrive at this equation, one can start with Maxwell's equations in a medium with no free charges and currents

$$\nabla \cdot \mathbf{D} = 0 \tag{2.1}$$

$$\nabla \cdot \mathbf{B} = 0 \tag{2.2}$$

$$\nabla \times \mathbf{E} = -\mu_0 \frac{\partial \mathbf{H}}{\partial t} \tag{2.3}$$

$$\nabla \times \mathbf{H} = \frac{\partial \mathbf{D}}{\partial t} \tag{2.4}$$

and the constitutive relations

$$\mathbf{D} = \epsilon_0 \mathbf{E} + \mathbf{P} \tag{2.5}$$

$$\mathbf{B} = \mu_0 \mathbf{H}. \tag{2.6}$$

4

The consititutive relation for **B** [Equation (2.6)] assumes that the material is nonmagnetic.

In a nonlinear medium, the polarization density **P** has a nonlinear dependence on the local electric field **E** [19]. When the fields are a discrete sum of monochromatic plane waves at different frequencies, **P** can be expressed in the powers of **E** as

$$\mathbf{P} \;=\; \epsilon_0[\chi^{(1)} \cdot \mathbf{E} + \mathbf{E} \cdot \chi^{(2)} \cdot \mathbf{E} + \mathbf{E} \cdot (\mathbf{E} \cdot \chi^{(3)} \cdot \mathbf{E}) + \cdots] \tag{2.7}$$

$$=\; \mathbf{P}^{(1)} + \mathbf{P}^{(2)} + \mathbf{P}^{(3)} + \cdots \tag{2.8}$$

where $\chi^{(1)}$ is the linear electric susceptibility tensor, $\chi^{(2)}$ is the second-order nonlinear susceptibility tensor, and so on. In materials that do not have a center of symmetry, $\chi^{(2)}$ is nonzero and higher order nonlinearities can usually be neglected. The focus of this thesis is on second-order nonlinear interactions in such materials.

The driven wave equation is obtained by taking the curl of Equation (2.3), and substituting Equation (2.4). For uniform plane waves, the driven wave equation can be simplified by using the vector identity $\nabla \times \nabla \times \mathbf{E} = \nabla(\nabla \cdot \mathbf{E}) - \nabla^2\mathbf{E}$, since $\nabla \cdot \mathbf{E} \equiv 0$ for a plane wave [19]. The driven wave equation then becomes

$$\nabla^2\mathbf{E} = \mu_0 \frac{\partial^2 \mathbf{D}}{\partial^2 t}. \tag{2.9}$$

It is convenient to split the linear and second-order nonlinear optical properties of the medium so that,

$$\mathbf{D} = \mathbf{D}^L + \mathbf{P}^{(2)} \tag{2.10}$$

where

$$\mathbf{D}^L = \epsilon_0\mathbf{E} + \mathbf{P}^{(1)} \tag{2.11}$$

is the linear part of **D**. With this separation, the driven wave equation takes the form

$$\nabla^2\mathbf{E} - \mu_0 \frac{\partial^2 \mathbf{D}^L}{\partial^2 t} = \mu_0 \frac{\partial^2 \mathbf{P}^{(2)}}{\partial^2 t}. \tag{2.12}$$

To put the driven wave equation in a form where we can interpret the effect of the second-order nonlinear polarization density, we consider the simple case of an isotropic medium, for which $\chi^{(1)}$ is a scalar quantity rather than a tensor. Then, the driven wave equation can be expressed as

$$\nabla^2\mathbf{E} - \frac{n^2}{c^2} \frac{\partial^2 \mathbf{E}}{\partial^2 t} = \mu_0 \frac{\partial^2 \mathbf{P}^{(2)}}{\partial^2 t} \tag{2.13}$$

where $n = \sqrt{1 + \chi^{(1)}}$ is the refractive index of the medium. The second-order nonlinear part of the polarization density acts as a source term in the driven wave equation and leads to the generation of new optical frequencies [19].

2.2 Coupled mode equations

In a second-order nonlinear medium, the nonlinear part of the polarization density is a quadratic function of the electric field, and the nonlinear interaction is between three waves that satisfy the frequency relation $\omega_3 = \omega_1 + \omega_2$ [19], [20]. For uniform plane waves propagating collinearly in the z-direction, the scalar form of Equation (2.13) is adequate. When these plane waves are also monochromatic, one can define complex amplitudes A by

$$E_m(z,t) = \mathrm{Re}[A_m e^{j(\omega_m t - k_m z)}] \qquad m = 1, 2, 3 \tag{2.14}$$

where $k_m = n_m \omega_m / c$ are the wavenumbers. The refractive indices n_m are allowed to be different for each wave since real materials are dispersive and the natural birefringence of anisotropic crystals is used for phase matching (see Section 2.3). We also represent the nonlinear polarization at each frequency as

$$P_m(z,t) = \mathrm{Re}[P_m e^{j\omega_m t}] \qquad m = 1, 2, 3. \tag{2.15}$$

The complex amplitude of the nonlinear polarization at each frequency can then be expressed as [19], [21]

$$P_1 = 2\epsilon_0 d_e A_3 A_2^* e^{-j(k_3 - k_2)z} \tag{2.16}$$

$$P_2 = 2\epsilon_0 d_e A_3 A_1^* e^{-j(k_3 - k_1)z} \tag{2.17}$$

$$P_3 = 2\epsilon_0 d_e A_1 A_2 e^{-j(k_1 + k_2)z} \tag{2.18}$$

where d_e is the effective nonlinear coefficient. The same nonlinear coefficient appears in all three nonlinear polarizations because we assume the material to be lossless [19].

We also assume that the variation of complex amplitudes in a distance of a wavelength is small and the relation

$$\left| \frac{d^2 A_m}{dz^2} \right| \ll \left| k_m \frac{dA_m}{dz} \right| \qquad m = 1, 2, 3 \tag{2.19}$$

is valid. This is called the slowly-varying envelope approximation [19] and is a very good approximation at optical frequencies. With this approximation, we obtain the coupled set of equations for the complex amplitudes

$$\frac{dA_1}{dz} = -j \frac{\omega_1 d_e}{n_1 c} A_3 A_2^* e^{-j\Delta k z} \tag{2.20}$$

$$\frac{dA_2}{dz} = -j \frac{\omega_2 d_e}{n_2 c} A_3 A_1^* e^{-j\Delta k z} \tag{2.21}$$

$$\frac{dA_3}{dz} = -j \frac{\omega_3 d_e}{n_3 c} A_1 A_2 e^{j\Delta k z} \tag{2.22}$$

6

where $\Delta k = k_3 - k_2 - k_1$ is the phase mismatch. These equations are called the coupled mode equations and they govern the evolution of the field amplitudes as the three waves interact through the second-order nonlinearity.

Different initial conditions at the input of the nonlinear medium lead to various frequency conversion processes. These SFG, SHG, and DFG. In the DFGprocess, one of the incident waves is amplified. If this aspect is more important for the application, the nonlinear process is called optical parametric amplification.

Second-order nonlinear interactions can also be viewed in terms of quantum mechanics, as three-photon interactions [20]. In SFG for example, two photons of energy $\hbar\omega_1$ and $\hbar\omega_2$ combine to form a photon of energy $\hbar\omega_3$. The frequency relation $\omega_3 = \omega_1 + \omega_2$ can then be interpreted as a statement of conservation of energy.

2.3 Phase matching

For a second-order interaction to be strong, the phase matching condition $\Delta k = 0$ has to be satisfied. When this condition is satisfied, the nonlinear polarization at each frequency travels with the same phase velocity as the electric field at that frequency [22]. In this case, the nonlinear polarization and the electric field at each frequency remain in phase throughout the interaction and the exchange of energy between the waves is efficient.

In terms of the quantum mechanical picture of second-order nonlinear interactions, the phase matching condition can be interpreted as momentum conservation. In SFG, the generated photon at ω_3 must have the same momentum $\hbar k_3$ as the sum of the momenta of the combined photons at ω_1 and ω_2.

The most common way of achieving phase matching is to employ the natural birefringence of nonlinear crystals [19], [23]. Recently, the method of quasi-phase matching has come into widespread use. This method has the potential to phase match any second-order nonlinear interaction, the only limitation being the transparency range of the nonlinear crystal [24], [25].

2.3.1 Birefringent phase matching

Most materials exhibit normal dispersion, that is, the refractive index a wave experiences increases with increasing frequency. The phase matching condition

7

expressed in the form

$$n_3\omega_3 = n_1\omega_1 + n_2\omega_2 \tag{2.23}$$

and the frequency relation $\omega_3 = \omega_1 + \omega_2$ cannot be simultaneously satisfied in a material with normal dispersion.

In an anisotropic crystal, there are two eigenmodes of polarization for any direction of propagation inside the crystal. These two modes are linearly polarized waves with orthogonal polarizations [20]. The orthogonally polarized eigenmodes experience different refractive indices, hence an anisotropic crystal displays birefringence. The refractive index an eigenmode experiences also changes with the direction of propagation inside the crystal. The phase matching condition can be satisfied by having one of the waves polarized orthogonally to the other two and by varying the direction of propagation inside the crystal. This is called birefringent phase matching (BPM).

In materials exhibiting normal dispersion, the highest frequency wave of the interaction has to be polarized along the fast axis of the crystal, the axis with the lower refractive index. The remaining possibilities for the direction of polarization of the two lower frequency waves lead to three different types of BPM. In this thesis, we follow the convention that the fields are labeled according to $\omega_1 < \omega_2 < \omega_3$. In type-I BPM, both the lower frequency waves at ω_1 and ω_2 are polarized along the slow axis, whereas in type-II (III) BPM, the lowest frequency wave at ω_1 is along the fast (slow) axis and the remaining wave at ω_2 is along the slow (fast) axis. These possibilities are summarized in Table 2.1 and Figure 2.1.

Type	$\omega_3 \rightarrow \omega_1 + \omega_2$
I	$f \rightarrow s + s$
II	$f \rightarrow f + s$
III	$f \rightarrow s + f$

Table 2.1: Potential phase matching types for BPM of second-order nonlinear interactions. Normal dispersion is assumed. The fast and slow axes are denoted by f and s, respectively.

2.3.2 Quasi-phase matching

Quasi-phase matching (QPM) is achieved in most cases by employing periodic domain reversals in ferroelectric crystals [24]. These domain reversals lead to a
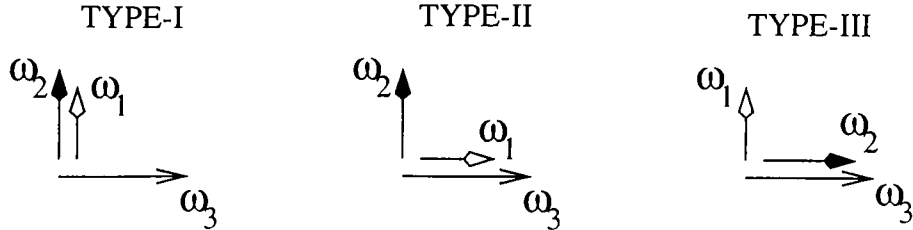
Figure 2.1: Polarization geometries for BPM types. The fast axis is horizontal and the slow axis is vertical.

periodic modulation of the sign of the effective nonlinear coefficient. The nonlinear coefficient then becomes a periodic function of z and can be represented by a Fourier series

$$d(z) = d_e \sum_{q=-\infty}^{\infty} G_q e^{jk_q z} \tag{2.24}$$

where $k_q = 2\pi q/\Lambda$ and Λ is the period of the modulation. In QPM, a particular spatial harmonic of the modulation compensates for the phase mismatch [24] and $k_3 - k_2 - k_1 - k_n$ becomes zero. The order n of this spatial harmonic gives a degree of freedom for phase matching. If the non-phase matched harmonics are ignored, the effective nonlinear coefficient of the quasi-phase matched interaction is equal to $d_e G_n$. With QPM, the highest frequency field of the interaction does not have to be polarized along the fast axis of the crystal anymore, and the number of potential phase matching types becomes eight. However, QPM is usually achieved with all fields polarized along the same direction, to take advantage of a large diagonal element of the second-order nonlinear susceptibility tensor $\chi^{(2)}$.

When the nonlinear coefficient is modulated by periodic sign reversal,

$$G_n = -\frac{2e^{-j\pi n\Gamma}}{n\pi} \sin(\pi n\Gamma) \tag{2.25}$$

where $\Gamma = l_Q/\Lambda$ is the duty cycle and l_Q is the length of the reversed domain in a single period [24]. The largest possible nonlinear coefficient is obtained by first-order QPM with 50% duty cycle and is equal to $2jd_e/\pi$.

2.4 Optical parametric amplification

In an OPA, an intense field at ω_3 amplifies a weak field at either ω_1 or ω_2. If either one of the lower frequency fields at ω_1 or ω_2 is not present initially, that field is generated in the interaction. In OPA terminology, the intense field at ω_3 is called the pump, the amplified field is called the signal, and the generated field

9

is called the idler. In this thesis, we assume for definiteness that the signal is at ω_2. However, the results presented below are equally valid if the signal is at ω_1.

In any second-order nonlinear interaction, the lack of one of the three interacting waves at the crystal input leads to field solutions whose intensities are independent of the relative phases of the two input fields. In an OPA, the idler field is absent at the crystal input, and the generated idler field adjusts its phase to match the phase difference between the pump and the signal. To show this result analytically, the coupled mode equations for the complex field amplitudes [Equations (2.20)-(2.22)] are first converted to equations for real field amplitudes and phases. We also normalize the real field amplitudes so that their squares correspond to photon flux densities. The transformation from the complex field amplitudes to real amplitudes a_i and phases ϕ_i for a phase matched interaction is

$$A_i = \sqrt{\frac{2\hbar\omega_i}{n_i c \epsilon_0}} a_i e^{-j\phi_i}. \tag{2.26}$$

The resulting real equations are

$$\frac{da_1}{dz} = -\kappa_a a_3 a_2 \sin\varphi \tag{2.27}$$

$$\frac{da_2}{dz} = -\kappa_a a_3 a_1 \sin\varphi \tag{2.28}$$

$$\frac{da_3}{dz} = \kappa_a a_1 a_2 \sin\varphi \tag{2.29}$$

$$\frac{d\varphi}{dz} = \kappa_a \left(\frac{a_1 a_2}{a_3} - \frac{a_2 a_3}{a_1} - \frac{a_1 a_3}{a_2} \right) \cos\varphi \tag{2.30}$$

where $\varphi = \phi_3 - \phi_2 - \phi_1$ [21]. In these equations, there is only a single coupling constant for the interaction

$$\kappa_a = d_e \sqrt{\frac{2\hbar}{c^3 \epsilon_0}} \sqrt{\frac{\omega_1 \omega_2 \omega_3}{n_1 n_2 n_3}}. \tag{2.31}$$

Substituting the real amplitude equations (2.27)-(2.29) into the phase equation (2.30) gives

$$\frac{d\varphi}{dz} = \frac{\cos\varphi}{\sin\varphi} \frac{d}{dz} \ln(a_1 a_2 a_3). \tag{2.32}$$

It may be verified by direct differentiation that this equation can be rewritten as

$$\frac{d}{dz} \ln(a_1 a_2 a_3 \cos\varphi) = 0. \tag{2.33}$$

Hence, $a_1 a_2 a_3 \cos\varphi$ is a conserved quantity; it does not depend on the propagation distance z. If one of the three fields has zero amplitude at the crystal entrance,

this quantity has a constant value of zero. Since the field that is not present initially is generated in the interaction, φ has to be equal to $\pm\pi/2$ throughout the interaction so that $\cos\varphi = 0$. In an OPA, the generated idler acquires a phase that makes φ equal to $-\pi/2$. In this case, the coupled mode equations that describe the interaction are

$$\frac{da_1}{dz} = \kappa_a a_3 a_2 \qquad (2.34)$$

$$\frac{da_2}{dz} = \kappa_a a_3 a_1 \qquad (2.35)$$

$$\frac{da_3}{dz} = -\kappa_a a_1 a_2. \qquad (2.36)$$

In terms of the quantum mechanical picture of second-order nonlinear interactions, when a signal photon is created, a pump photon is annihilated and an idler photon is created [19], [20]. The Manley-Rowe relations express the conserved quantities

$$C_1 = a_1^2(z) + a_3^2(z) = a_3^2(0) \qquad (2.37)$$

$$C_2 = a_2^2(z) + a_3^2(z) = a_2^2(0) + a_3^2(0) \qquad (2.38)$$

in terms of the photon flux densities [19], [20]. These quantities can be used to transform the coupled mode equations for an OPA [Equations (2.34)–(2.36)] to a single differential equation which can be integrated to obtain the solutions for field amplitudes in terms of Jacobi elliptic functions. We define a new variable $\theta(z)$ through

$$a_1(z) = \sqrt{C_1} \cos\theta(z) \qquad (2.39)$$

$$a_3(z) = \sqrt{C_1} \sin\theta(z). \qquad (2.40)$$

Since no idler is present at the crystal input, $\theta(0)$ is equal to an odd multiple of $\pi/2$; for convenience, we choose $\theta(0) = \pi/2$. Substituting into Equation (2.34), the signal field amplitude is obtained as

$$a_2(z) = -\frac{1}{\kappa_a}\frac{d\theta}{dz}. \qquad (2.41)$$

We then substitute Equation (2.41) into the Manley-Rowe relation for C_2 [Equation (2.38)] to get a single differential equation

$$\frac{1}{\kappa_a^2}\left(\frac{d\theta}{dz}\right)^2 + C_1 \sin^2(\theta) = C_2 \qquad (2.42)$$

11

in the variable $\theta(z)$. When integrated, Equation (2.42) gives

$$\int_{\pi/2}^{\theta}(1 - m_a \sin^2 \psi)^{-1/2}d\psi = -\kappa_a\sqrt{C_2}z \tag{2.43}$$

where $m_a = C_1/C_2$. This integral can be expressed in terms of the elliptic integral of the first kind [26], whose inversion leads to Jacobi elliptic functions. The integral first has to be put into a standard elliptic integral form so that its lower limit is zero. This leads to

$$\int_{0}^{\theta}(1 - m_a \sin^2 \psi)^{-1/2}d\psi = K(m_a) - \kappa_a\sqrt{C_2}z = Z_a \tag{2.44}$$

where

$$K(m_a) = \int_{0}^{\pi/2}(1 - m_a \sin^2 \psi)^{-1/2}d\psi \tag{2.45}$$

is the complete elliptic integral of the first kind, and is also the quarter-period of Jacobi elliptic functions [26]. The angle θ, whose value at the crystal output is unknown, is called the amplitude and m_a is called the parameter in elliptic function terminology [26]. The Jacobi elliptic function sn is defined in terms of the amplitude θ as $\text{sn}(Z_a|m_a) = \sin\theta$. We then obtain the solutions for the field amplitudes as

$$a_1(z) = \sqrt{C_1}\,\text{cn}(Z_a|m_a) \tag{2.46}$$

$$a_2(z) = \sqrt{C_2}\,\text{dn}(Z_a|m_a) \tag{2.47}$$

$$a_3(z) = \sqrt{C_1}\,\text{sn}(Z_a|m_a) \tag{2.48}$$

where the Jacobi elliptic functions cn and dn are defined as $\text{cn}(Z_a|m_a) = \cos\theta$ and $\text{dn}(Z_a|m_a) = 1 - m_a\text{sn}^2(Z_a|m_a)$; respectively.

Figure 2.2 shows the evolution of the photon flux densities in an OPA, computed using the solutions (2.46)–(2.48). The photon flux densities are normalized to the incident pump photon flux density $a_3^2(0)$. We define a dimensionless normalized propagation distance $\xi = \kappa_a a_3(0)z$ so that the results are presented in a more general fashion. For this example, the input signal photon flux density is 0.25 times the input pump photon flux density, and therefore, $m_a = 4/5$. As shown in Figure 2.2, the signal field is amplified in the interaction until the pump field is fully depleted. At this point, the argument Z_a of the Jacobi elliptic functions becomes equal to zero [26]. Afterwards, the interaction reverses direction, and the signal photons combine with the idler photons to regenerate the pump. This SFG process is called back-conversion. The interaction continues in this fashion and the three fields exchange energy periodically as they propagate in the nonlinear crystal.

12
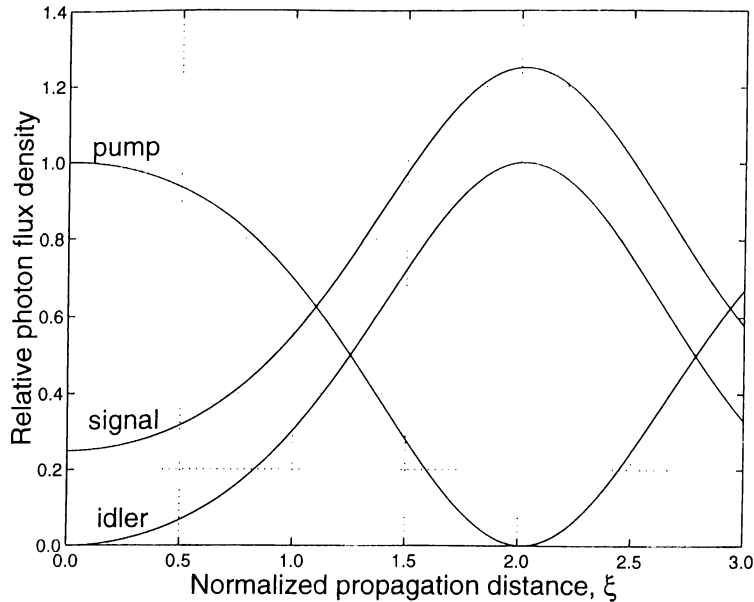
Figure 2.2: The evolution of the pump, signal, and idler photon flux densities in an OPA as functions of the normalized propagation distance ξ. All photon flux densities are normalized to the incident pump photon flux density. The input signal photon flux density is 0.25 times the input pump photon flux density.

2.5 Optical parametric oscillation

An OPO is constructed by placing the OPA crystal inside a resonator. If the resonator mirrors reflect only at the signal frequency, the OPO is singly-resonant. Singly-resonant OPO's are preferred to doubly-resonant OPO's (in which both the signal and the idler are resonated), primarily because the phase-insensitive OPA interaction in a singly-resonant OPO results in stable operation. However, doubly-resonant OPO's have a significantly lower threshold pump intensity. They are therefore employed if the available peak pump intensity is limited.

In a singly-resonant OPO, one of the mirrors is a partial reflector at the signal frequency in order to couple the signal out of the resonator. If the small-signal (unsaturated) gain is larger than the total cavity loss (output coupling and parasitic useless losses combined), oscillation starts and the signal field intensity starts to grow. The initial signal intensity is usually provided by spontaneous parametric fluorescence [27], not by a laser at the signal frequency. The OPO reaches steady-state when the saturated signal gain compensates for the loss exactly. The steady-state oscillation condition is

$$R\frac{a_2^2(l)}{a_2^2(0)} = 1 \qquad (2.49)$$

13
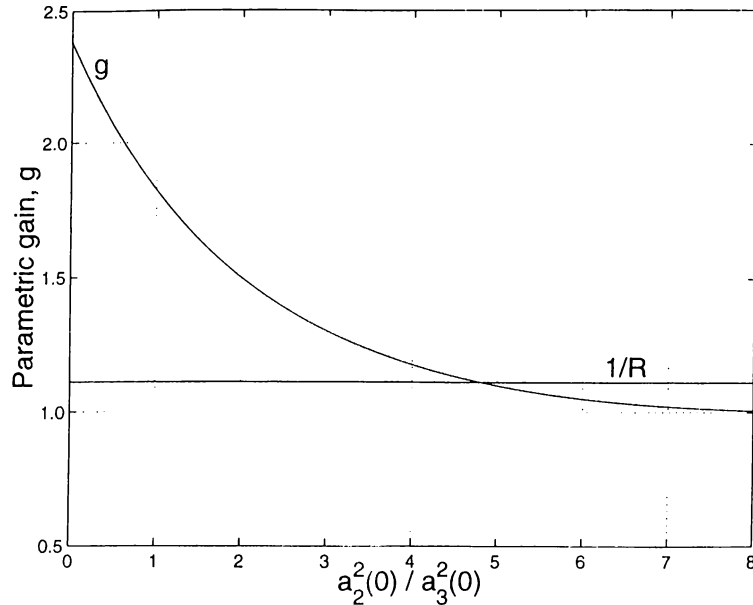
Figure 2.3: The intracavity signal flux density of an OPO is found by the intersection of the gain saturation curve and the resonator loss line (of value $1/R$). For this example, the nonlinear drive of the OPO is unity and the lumped resonator reflectance $R = R_{OC}R_L$ is 0.9. The signal flux density is normalized to the input pump flux density.

where $R = R_{OC}R_L$; R_{OC} is the reflectance of the output coupler, R_L is a lumped reflectance representing useless losses, and l is the crystal length.

To find the intracavity signal photon flux density $a_2^2(0)$, in general one has to solve Equation (2.49) iteratively using a numerical root-finding algorithm. In this thesis, the secant method is used for finding the root of the function $f[a_2^2(0)] = Ra_2^2(l)/a_2^2(0) - 1$. The secant method starts with two initial guesses on $a_2^2(0)$. At each iteration, the saturated signal gain $g = a_2^2(l)/a_2^2(0)$ is calculated using the single-pass solutions [Equations (2.46)–(2.48)] and the next approximation to $a_2^2(0)$ is taken to be the zero-crossing of the line that passes through the two previous approximations [28]. The algorithm stops when the difference between the last two approximations is less than a specified tolerance.

Figure 2.3 shows an example of gain saturation for the signal field as a function of the intracavity signal photon flux density. The gain saturation in an OPA is completely characterized by the dimensionless parameter $D = [\kappa_a a_3(0)l]^2$, called the nonlinear drive [10], [23], [17]. The nonlinear drive is a measure of the strength of the interaction. In Figure 2.3, the nonlinear drive is chosen to be unity and this results in a small-signal gain of 2.4.

In the small-signal regime, the depletion of the pump field is negligible. Therefore, the small-signal gain g_0 can be obtained by solving the coupled mode equations [Equations (2.34)–(2.36)] with a_3 taken to be constant. In this regime,

$$a_2(z) = a_2(0)\cosh[\kappa_4 a_3(0)z] \tag{2.50}$$

and the small-signal gain is $g_0 = \cosh^2(\sqrt{D})$. The threshold nonlinear drive D_{th} can be found by solving $Rg_0 = 1$ for D.

Also shown on Figure 2.3 is a loss line representing a resonator loss of $R = 0.9$. The intersection of the gain saturation curve and the loss line gives the intracavity signal flux density. For this example, the intracavity signal flux density is 4.8 times the input pump flux density. Once the intracavity signal flux density is known, the field amplitudes at the crystal output can be calculated using the single-pass solutions [Equations (2.46)–(2.48)].

The performance of an OPO is characterized by the photon conversion efficiency (also called the quantum efficiency [10], [23])

$$\eta = \frac{(1 - R_{\mathrm{OC}})a_2^2(l)}{a_3^2(0)} \tag{2.51}$$

the ratio of the signal photon flux density coupled out of the cavity to the input pump photon flux density. Figure 2.4 shows the conversion efficiency of the OPO as a function of the nonlinear drive for four different values of the output coupler reflectance R_{OC}. For each case, $R_{\mathrm{L}} = 1$. The OPO can be very efficient, with conversion efficiencies reaching 100% for particular values of the nonlinear drive. These maxima of conversion correspond to complete depletion of the pump. If the nonlinear drive is increased still further, the conversion efficiency drops because of back-conversion. Note that for a given value of the nonlinear drive, the output coupler reflectance can be optimized for maximum conversion [10], [23]. Figure 2.5 shows the dependence of the optimum R_{OC} on the nonlinear drive. The optimum R_{OC} decreases monotonically with increasing nonlinear drive.

2.6 Sum-frequency generation

In SFG, a lower frequency input field at ω_4 and a higher frequency input field at ω_5 interact to generate their sum-frequency at $\omega_6 = \omega_4 + \omega_5$. As in the OPA case, the lack of a sum-frequency field at the crystal input leads to phase-insensitive field solutions; the generated sum-frequency field acquires a phase so
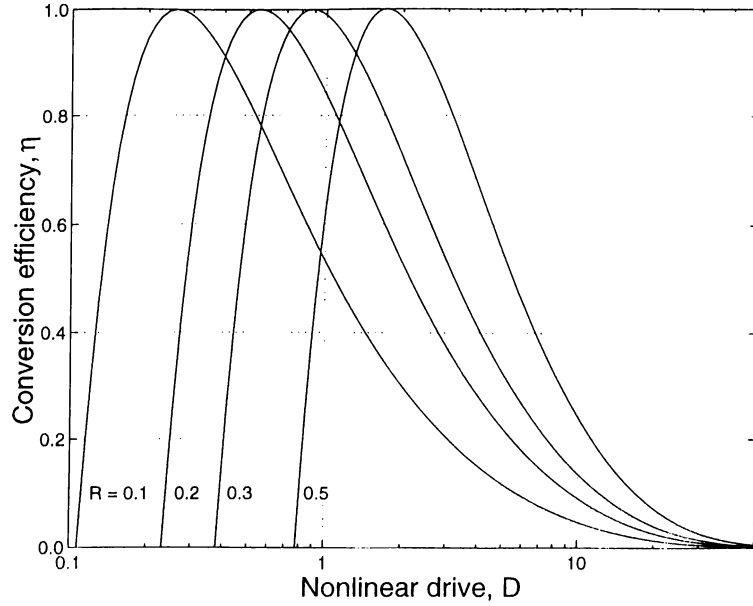
Figure 2.4: Photon conversion efficiency of the OPO as a function of the nonlinear drive for four different values of R_{OC}. R_L is taken to be unity.
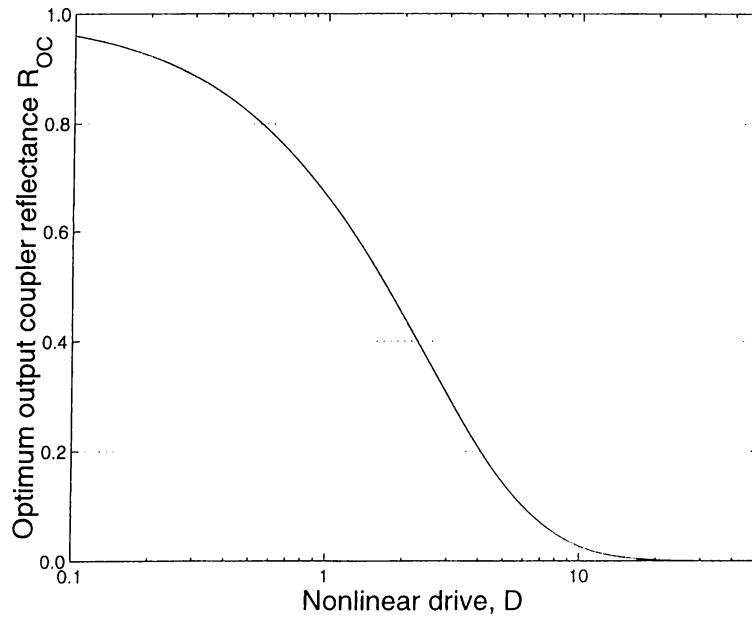
Figure 2.5: Optimum output coupler reflectance R_{OC} for the OPO as a function of the nonlinear drive. R_L is taken to be unity.

that $\varphi = \phi_6 - \phi_5 - \phi_4 = \pi/2$. The coupled mode equations that govern the interaction are

$$\frac{da_4}{dz} = -\kappa_b a_6 a_5 \tag{2.52}$$

$$\frac{da_5}{dz} = -\kappa_b a_6 a_4 \tag{2.53}$$

$$\frac{da_6}{dz} = \kappa_b a_4 a_5 \tag{2.54}$$

with the coupling constant

$$\kappa_b = d_e \sqrt{\frac{2\hbar}{c^3 \epsilon_0}} \sqrt{\frac{\omega_4 \omega_5 \omega_6}{n_4 n_5 n_6}} \,. \tag{2.55}$$

The solutions for the SFG process are in terms of Jacobi elliptic functions as in OPA's. However, the SFG solutions depend on which of the two input fields has smaller photon flux density at the crystal input. The interaction reverses direction when the field with the smaller photon flux density is fully depleted inside the crystal, and back-conversion (parametric amplification) begins. If $a_4^2(0) > a_5^2(0)$, the solutions are [17]

$$a_4(z) = \sqrt{C_1} \, \mathrm{dn}(Z_b | m_b) \tag{2.56}$$

$$a_5(z) = \sqrt{C_2} \, \mathrm{cn}(Z_b | m_b) \tag{2.57}$$

$$a_6(z) = \sqrt{C_2} \, \mathrm{sn}(Z_b | m_b) \tag{2.58}$$

where

$$C_1 = a_4^2(z) + a_6^2(z) = a_4^2(0) \tag{2.59}$$

$$C_2 = a_5^2(z) + a_6^2(z) = a_5^2(0) \tag{2.60}$$

are the Manley-Rowe conserved quantities and

$$Z_b = \kappa_b \sqrt{C_1} \, z \tag{2.61}$$

$$m_b = \frac{C_2}{C_1} \,. \tag{2.62}$$

The solutions for the case $a_5^2(0) > a_4^2(0)$ are obtained by interchanging the field subscripts 4 and 5 and the Manley-Rowe subscripts 1 and 2.

Figure 2.6 shows the evolution of photon flux densities in SFG for the case $a_4^2(0) > a_5^2(0)$. All photon flux densities are normalized to $a_4^2(0)$. The higher frequency SFG input field is completely depleted at $Z_b = 2.3$, at which point the sum-frequency photon flux density reaches its maximum value. After this point, back-conversion of the sum-frequency to the SFG input fields begins and the SFG photon flux density decreases.

2.7 Second-harmonic generation

In SHG, an incident field at ω leads to the generation of light at 2ω. The incident field at ω is called the fundamental and the generated field at 2ω is called

17
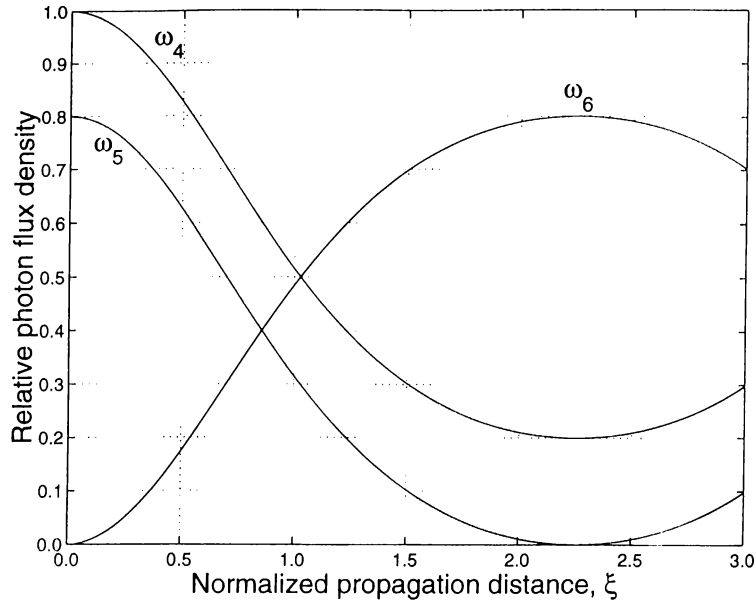
Figure 2.6: The evolution of the lower frequency SFG input (a_4), higher frequency SFG input (a_5), and sum-frequency (a_6) photon flux densities as functions of the normalized propagation distance ξ. All photon flux densities are normalized to $a_4^2(0)$.

the second-harmonic. SHG can also be viewed as SFG degenerate in frequency ($\omega_4 = \omega_5 = \omega$). However, the phase matching type may require the fundamental field to have two components polarized along orthogonal eigenmodes of the crystal. In type-II phase matched SHG, the fundamental field is nondegenerate in polarization. In other words, the fundamental has two orthogonally polarized components a_4 and a_5. In this case, the coupled mode equations are the same as the equations for SFG [Equations (2.52)–(2.54)]. The usual practice in non-degenerate SHG is to orient a linearly polarized fundamental field at a $45°$ angle to the two eigenpolarization directions since maximum conversion to the second-harmonic takes place if the incident fundamental components have the same photon flux density. For this orientation, the SHG process becomes degenerate and this degeneracy reduces the number of coupled mode equations to two [19].

In type-I phase matched SHG, the fundamental field is degenerate in both frequency and polarization; the fundamental field is polarized along the slow axis of the crystal and it cannot be decomposed into two distinct fields corresponding to $\omega_4 = \omega$ and $\omega_5 = \omega$. In terms of normalized real field amplitudes, the equations

18

that govern degenerate SHG are

$$\frac{da_4}{dz} = -\kappa_b a_6 a_4 \tag{2.63}$$

$$\frac{da_6}{dz} = \frac{1}{2}\kappa_b a_4^2 \tag{2.64}$$

with the coupling constant

$$\kappa_b = d_e \sqrt{\frac{2\hbar}{c^3\epsilon_0}} \sqrt{\frac{2\omega^3}{n_4^2 n_6}} \tag{2.65}$$

where a_4 is the fundamental at ω and a_6 is the second-harmonic at 2ω. The solutions to this set of equations are [19]

$$a_4(z) = a_4(0)\text{sech}\,\xi \tag{2.66}$$

$$a_6(z) = \frac{1}{\sqrt{2}}a_4(0)\tanh\xi \tag{2.67}$$

where

$$\xi = \frac{1}{\sqrt{2}}\kappa_b a_4(0)z \tag{2.68}$$

is the normalized propagation distance. There is only one Manley-Rowe conserved quantity for SHG, and this quantity

$$C_1 = a_4^2(z) + 2a_6^2(z) = a_4^2(0) \tag{2.69}$$

is proportional to the total intensity in the interaction.

Figure 2.7 shows the evolution of the photon flux densities along the direction of propagation inside the crystal for SHG. Both photon flux densities are normalized to the incident fundamental photon flux density. In contrast to other second-order nonlinear interactions, the photon flux densities do not evolve periodically in degenerate SHG. The second-harmonic photon flux density increases monotonically, and all of the input fundamental flux density is converted to the second-harmonic in the limit of infinite interaction length.
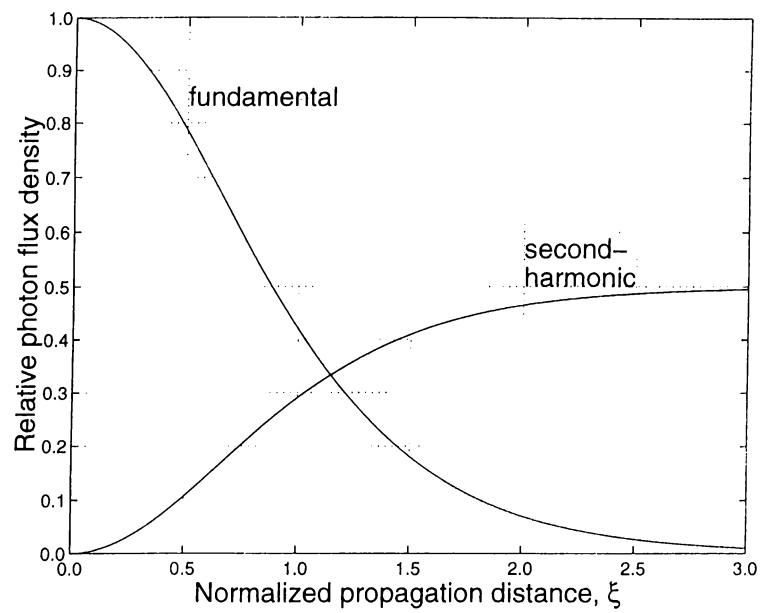
Figure 2.7: The evolution of the fundamental and the second-harmonic photon flux densities in SHG as functions of the normalized propagation distance ξ. Both photon flux densities are normalized to the incident fundamental photon flux density.

Chapter 3

Simultaneous Phase Matching of OPO and SFG/SHG

Single-crystal upconversion OPO's are based on the premise that two second-order nonlinear interactions can be phase matched for the same direction of propagation inside the same crystal [29], [30]. For frequency upconversion with an OPO, the second nonlinear interaction has to be either SHG or SFG. Upconversion with the OPO is more efficient if the SFG or the SHG processes take advantage of the high intensity of the resonant signal field.

The simultaneous phase matching condition can be satisfied by either BPM or QPM of the two processes. Various combinations of phase matching types of the two processes lead to several classes of upconversion OPO's, each governed by a different set of coupled mode equations. Some of these classes require a polarization rotation for the signal or the pump fields.

Simultaneous phase matching of two second-order interactions within a single nonlinear crystal has been experimentally demonstrated for a number of frequency conversion applications. Single-crystal upconversion OPO's that employ simultaneous BPM of frequency doubling [8] or SFG [9] in $KTiOPO_4$ (KTP), and periodically poled lithium niobate (PPLN) OPO's with simultaneous third-order QPM of frequency doubling [31], [32] or SFG [33] have been reported. A cascaded OPO, where the signal of a primary OPO acts as the pump for a secondary OPO, has been demonstrated in PPLN with first-order QPM for both OPO processes [34]. Simultaneous SFG of the pump and the idler in a β-barium borate (BBO) crystal OPA has been achieved with BPM [35]. Simultaneous SFG with BPM has also been reported in an ADP crystal parametric fluorescence experiment [36].

Third-harmonic generation in PPLN with simultaneous first-order QPM of the frequency doubling and SFG processes has also been demonstrated [37].

For each combination of phase matching types for the OPO and SHG/SFG processes, the respective coupling constants κ_a and κ_b depend on the phase-matched frequencies, the refractive indices, and the effective nonlinear coefficients. The ratio of the two coupling constants $\beta = \kappa_b/\kappa_a$ is an important quantity that may assume a range of values depending on these parameters. Here, the relative magnitudes of the frequencies and effective nonlinear coefficients are of particular importance. If the OPO and SHG/SFG processes are of the same BPM type, the effective nonlinear coefficients differ only due to dispersion of the second-order nonlinearity [38]. However, for different phase matching types the effective nonlinear coefficients may be dramatically different from each other.

If QPM is employed for simultaneous phase matching, the QPM order of the two processes may or may not be different from each other. Since the effective nonlinear coefficient for a process depends on the QPM order as well as the other parameters mentioned above, choosing different QPM orders for the two processes provides a mechanism for adjusting the value of β. The results of Chapter 5 show that having some control on the value of β can be very useful in maximizing the conversion efficiency of single-crystal upconversion OPO's.

Note that QPM can easily be used to phase match two interactions in a single crystal by employing two consecutive sections with different poling periods. Such a double-grating PPLN was recently used for intracavity SFG of an OPO [39]. However, these double-grating devices are identical to upconversion OPO's with two different crystals in terms of the plane-wave theory [18], [17].

3.1 Simultaneous phase matching of OPO and SFG

We first present the possible combinations of BPM types for OPO's with simultaneous SFG. These combinations lead to four different classes of sum-frequency generating OPO's (SF-OPO's), some of which require a polarization rotation for the signal or the pump fields. QPM opens up several more possibilities of phase matching type combinations, yet, each of these combinations can be identified with one of the four SF-OPO classes.

3.1.1 Birefringent phase matching

There are nine possible combinations of BPM types for the OPO and SFG processes. These combinations are summarized in Table 3.1 and Figure 3.1. In this thesis, the resonant signal field, which also constitutes the lower frequency input field for the SFG process, is labeled as being at ω_2. However, our formulation and results are equally valid if the field at ω_1 is resonated and used as a SFG input.

| | OPO | SFG |
Type	$\omega_3 \rightarrow \omega_1 + \omega_2$	$\omega_2 + \omega_3 \rightarrow \omega_6$
I	$f \rightarrow s + s$	$s + s \rightarrow f$
II	$f \rightarrow f + s$	$f + s \rightarrow f$
III	$f \rightarrow s + f$	$s + f \rightarrow f$

Case	OPO	SFG	Rotation	Class
1	I	I	pump	C
2	II	I	pump	C
3	III	I	both	B
4	I	II	both	B
5	II	II	both	B
6	III	II	pump	C
7	I	III	none	A
8	II	III	none	A
9	III	III	signal	D

Table 3.1: Possible combinations of BPM types for OPO with simultaneous SFG. Normal dispersion is assumed. The fast and slow axes are denoted by f and s, respectively.

In cases 7 and 8, the pump and the signal fields are polarized along the same axes in both the OPO and SFG processes. As a result, the two processes become coupled through the signal and the pump fields. The set of coupled mode equations that describe this interaction are

$$\frac{da_1}{dz} = \kappa_a a_3 a_2 \tag{3.1}$$

$$\frac{da_2}{dz} = \kappa_a a_3 a_1 - \kappa_b a_6 a_3 \tag{3.2}$$

$$\frac{da_3}{dz} = -\kappa_a a_1 a_2 - \kappa_b a_6 a_2 \tag{3.3}$$

$$\frac{da_6}{dz} = \kappa_b a_2 a_3 . \tag{3.4}$$
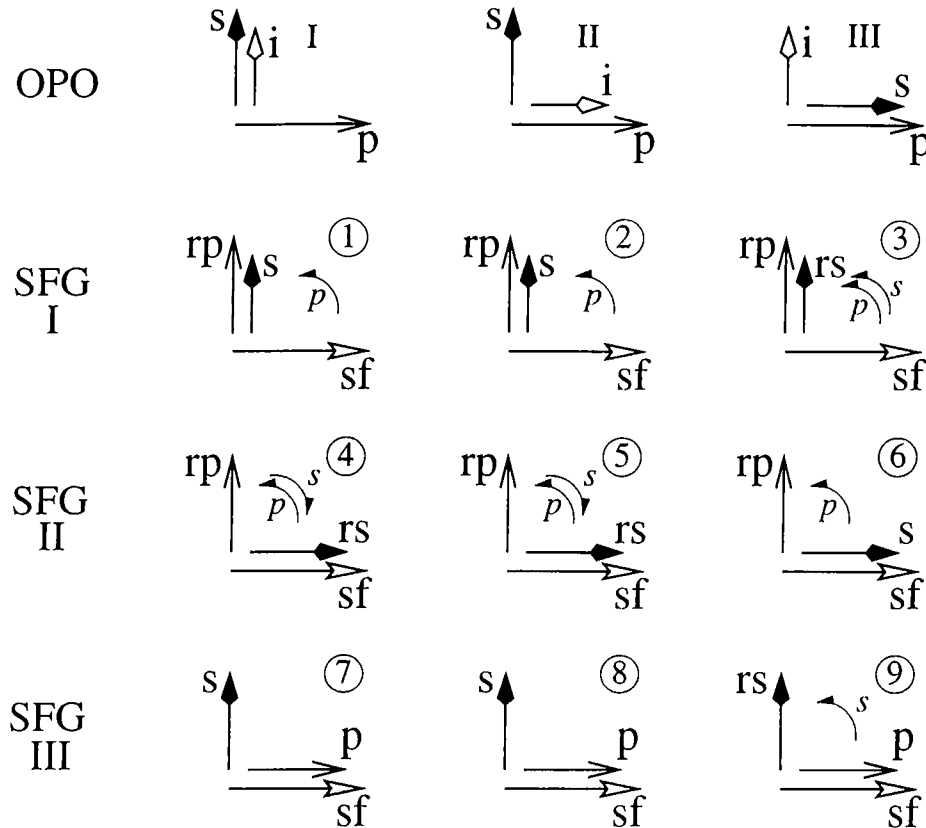
Figure 3.1: Polarization diagrams for possible combinations of BPM types in SF-OPO's. The fast axis is horizontal and the slow axis is vertical. Polarizations for the pump (p), signal (s), idler (i), polarization rotated pump (rp), polarization rotated signal (rs), and sum-frequency (sf) are shown. Intracavity polarization rotation is indicated with an arc. Each combination of phase matching types is labeled with a circled number.

We arrive at these equations by combining the OPA equations [Equations (2.34)–(2.36)] with the SFG equations [Equations (2.52)–(2.54)]. The signal a_2 (pump a_3) and the lower frequency SFG input a_4 (higher frequency SFG input a_5) are the same field mode; the rate of change of the signal (pump) field amplitude is the sum of the rates of change of the OPO signal (pump) and the lower (higher) frequency SFG input field amplitudes separately. The same equations can also be obtained by considering the total nonlinear polarization P_2 and P_3 at ω_2 and ω_3, respectively, and re-deriving the coupled mode equations. We designate this SF-OPO process as class-A.

In cases 3, 4, and 5 the pump and signal fields are both orthogonally polarized between the OPO and SFG processes. The same crystal can be used for both processes at the same time through extracavity polarization rotation of the pump and intracavity polarization rotation of the signal. However, the two processes

are not coupled in the crystal as they are in class-A interactions, and the coupled mode equations that govern this SF-OPO are simply Equations (2.34)–(2.36) and (2.52)–(2.54). We designate this SF-OPO as class-B.

In cases 1, 2, and 6, the pump field is polarized orthogonally between the OPO and SFG processes. A polarization rotation of the pump at the cavity input is required for SFG to take place. The signal field is common to both processes, and couples them to each other. The set of coupled mode equations that describe all three cases are

$$\frac{da_1}{dz} = \kappa_a a_3 a_2 \tag{3.5}$$

$$\frac{da_2}{dz} = \kappa_a a_3 a_1 - \kappa_b a_6 a_5 \tag{3.6}$$

$$\frac{da_3}{dz} = -\kappa_a a_1 a_2 \tag{3.7}$$

$$\frac{da_5}{dz} = -\kappa_b a_6 a_2 \tag{3.8}$$

$$\frac{da_6}{dz} = \kappa_b a_2 a_5 \,. \tag{3.9}$$

We designate this SF-OPO process as class-C.

In case 9, the signal is orthogonally polarized between the OPO and SFG processes, and an intracavity polarization rotation of the signal is necessary. The OPO and SFG processes are coupled to each other through the pump, which is common to both processes inside the crystal. The coupled mode equations that describe the interaction are

$$\frac{da_1}{dz} = \kappa_a a_3 a_2 \tag{3.10}$$

$$\frac{da_2}{dz} = \kappa_a a_3 a_1 \tag{3.11}$$

$$\frac{da_3}{dz} = -\kappa_a a_1 a_2 - \kappa_b a_6 a_4 \tag{3.12}$$

$$\frac{da_4}{dz} = -\kappa_b a_6 a_3 \tag{3.13}$$

$$\frac{da_6}{dz} = \kappa_b a_3 a_4 \,. \tag{3.14}$$

We designate this SF-OPO process as class-D.

3.1.2 Quasi-phase matching

In terms of simultaneous phase matching of SFG in an OPO, the eight QPM phase matching types lead to 64 different combinations. We found that each of

these combinations can be identified with one of the four classes introduced above, depending on whether the coupling between the two processes in the crystal is through the signal (class-C), the pump (class-D), both (class-A), or neither (class-B).

3.2 Simultaneous phase matching of OPO and SHG

The possible combinations of BPM types for OPO with simultaneous SHG lead to three different classes of self-doubling OPO's (SD-OPO's). Two of these classes require a polarization rotation for the signal field while the third does not. We also find that each of the possible combinations of QPM types can be identified with one of these three classes.

3.2.1 Birefringent phase matching

There are six possible combinations of BPM types for the OPO and SHG processes. These combinations are summarized in Table 3.2 and Figure 3.2. The fundamental field for SHG is assumed to be the resonant signal field, since the high intracavity signal intensity leads to efficient SHG. For frequency upconversion with the SD-OPO, the signal field has to be at ω_2, so that $2\omega_2 > \omega_3$ can be satisfied.

In cases 1 and 2, the OPO signal and the SHG fundamental are both polarized along the same direction and the two fields are indistinguishable in every aspect. As a result, the two processes are coupled through the signal field which is common to the two processes. The coupled mode equations that govern this interaction are

$$\frac{da_1}{dz} = \kappa_a a_3 a_2 \tag{3.15}$$

$$\frac{da_2}{dz} = \kappa_a a_3 a_1 - \kappa_b a_6 a_2 \tag{3.16}$$

$$\frac{da_3}{dz} = -\kappa_a a_1 a_2 \tag{3.17}$$

$$\frac{da_6}{dz} = \frac{1}{2}\kappa_b a_2^2 \tag{3.18}$$

where κ_a and κ_b are the coupling constants for the OPA and the SHG processes,

26

| | OPO | SHG |
Type	$\omega_3 \to \omega_1 + \omega_2$	$\omega_2 + \omega_2 \to 2\omega_2$
I	$f \to s + s$	$s + s \to f$
II	$f \to f + s$	$s + f \to f$
III	$f \to s + f$	

Case	OPO	SHG	Rotation	Class
1	I	I	no	A
2	II	I	no	A
3	III	I	yes	B
4	I	II	yes	C
5	II	II	yes	C
6	III	II	yes	C

Table 3.2: Possible combinations of BPM types for OPO with simultaneous SHG. Normal dispersion is assumed. The fast and slow axes are denoted by f and s, respectively. There is no type-III BPM for SHG since this process is degenerate in frequency.
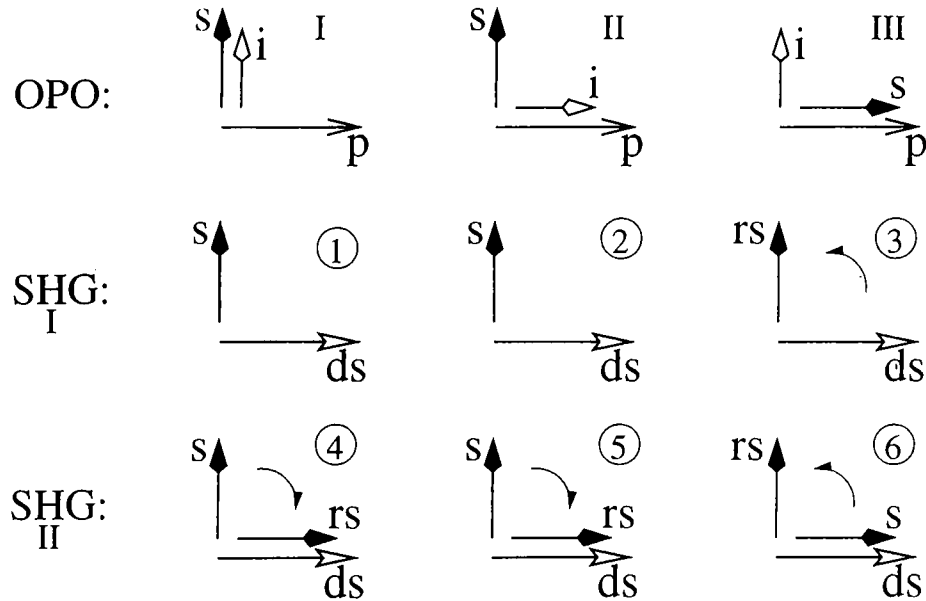
Figure 3.2: Polarization diagrams for possible combinations of BPM types in SD-OPO's. The fast axis is horizontal and the slow axis is vertical. Polarizations for the pump (p), signal (s), idler (i), polarization rotated signal (rs), and frequency-doubled signal (ds) are shown. Intracavity polarization rotation is indicated with an arc. Each combination of phase matching types is labeled with a circled number.

respectively. We obtain these equations by combining the OPA equations [Equations (2.34)–(2.36)] with the degenerate SHG equations [Equations (2.63)–(2.64)].

27

We designate this SD-OPO process as class-A.

In case 3, the polarizations of the OPO signal and the SFG fundamental are orthogonal. However, an intracavity polarization rotation of the signal provides the input field for SHG and allows the same crystal to be used for both processes at the same time. In contrast with class-A SD-OPO's, the two processes are not coupled in the crystal, and the coupled mode equations that describe the interaction are simply Equations (2.34)–(2.36) and (2.63)–(2.64). We designate this SD-OPO as class-B.

In cases 4, 5, and 6, the SHG process is nondegenerate in polarization, and there are two orthogonally polarized fundamental components. The OPO signal is polarized along either component of the fundamental in each case, and the two processes are coupled through this component. An intracavity polarization rotation of the signal field provides the second fundamental component and makes SHG possible. The coupled mode equations that govern the interaction are

$$\frac{da_1}{dz} = \kappa_a a_3 a_2 \tag{3.19}$$

$$\frac{da_2}{dz} = \kappa_a a_3 a_1 - \kappa_b a_6 a_5 \tag{3.20}$$

$$\frac{da_3}{dz} = -\kappa_a a_1 a_2 \tag{3.21}$$

$$\frac{da_5}{dz} = -\kappa_b a_6 a_2 \tag{3.22}$$

$$\frac{da_6}{dz} = \kappa_b a_2 a_5. \tag{3.23}$$

These equations are obtained by combining the OPA equations [Equations (2.34)–(2.36)] with the nondegenerate SHG equations [Equations (2.52)–(2.54)]. We designate this SD-OPO as class-C. Note that Equations (3.19)–(3.23) are the same as the coupled mode equations that govern class-C SF-OPO's [Equations (3.5)–(3.9)].

3.2.2 Quasi-phase matching

Since the SHG process is degenerate in frequency, there are only six possible QPM types for SHG as opposed to eight for the OPO. In terms of simultaneous phase matching of SHG in an OPO, the potential QPM types lead to 48 different combinations. We found that each of these combinations can be identified with one of the three classes introduced above, depending on whether the SHG process is nondegenerate in polarization (class-C) and if not, whether the polarizations

28

of the OPO signal and the SHG fundamental are orthogonal (class-B) or not (class-A).

Chapter 4

Single-Pass Solutions

To analyze the performance of single-crystal upconversion OPO's, it is first necessary to calculate the single-pass parametric gain for the signal field by solving the coupled mode equations for each class [29], [30]. For some of these classes, analytical solutions of the coupled mode equations are available. For the other classes however, we used a numerical method to compute the single-pass parametric gain. For these classes, the coupled mode equations were solved with the Runge-Kutta-Fehlberg method.

Runge-Kutta-Fehlberg is an adaptive step-size method widely used for solving ordinary differential equations [28]. At each step, this technique uses two fixed step-size Runge-Kutta methods with orders five and four, to estimate the step-size that will keep the local error within a specified tolerance. Having a small local error at each step ensures that the global error is also small. In our calculations, the tolerance is chosen to be 10^{-5} times the input signal field amplitude.

4.1 Single-pass solutions of SF-OPO's

The coupled mode equations for two of the four SF-OPO classes have analytical solutions. A simple transformation maps the class-A equations to regular OPA equations, leading to analytical solutions in terms of Jacobi elliptic functions. In class-B SF-OPO's the OPA and SFG processes are not coupled in the crystal, and analytical solutions are readily available. For class-C and class-D SF-OPO's, however, we used the Runge-Kutta-Fehlberg method to solve the coupled mode equations.

4.1.1 Class-A solutions

An important simplification in the coupled mode equations for class-A SF-OPO's is achieved by recognizing that the right hand sides of Equations (3.1) and (3.4) are proportional. Since both the idler field a_1 and the sum-frequency field a_6 have zero amplitudes at the crystal input, we have $a_6(z) = \beta a_1(z)$. The coupled mode equations then become

$$\frac{da_1}{dz} = \kappa_a a_3 a_2 \tag{4.1}$$

$$\frac{da_2}{dz} = (1 - \beta^2)\kappa_a a_3 a_1 \tag{4.2}$$

$$\frac{da_3}{dz} = -(1 + \beta^2)\kappa_a a_1 a_2 . \tag{4.3}$$

The evolution of the field amplitudes as they propagate down the crystal depends on the value of β. If β is equal to unity, the right hand side of Equation (4.2) becomes equal to zero for all values of z. In this case, the parametric gain provided by the pump is exactly balanced by the nonlinear loss due to SFG, and the signal field amplitude stays constant throughout the length of the crystal. If β is less than unity, the parametric gain overcomes the nonlinear SFG loss, and the signal field is amplified. Under this condition, the substitutions $a_1 = u_1/\sqrt{(1 - \beta^2)(1 + \beta^2)}$, $a_2 = u_2/\sqrt{1 + \beta^2}$, and $a_3 = u_3/\sqrt{1 - \beta^2}$ transform Equations (4.1)–(4.3) to the coupled mode equations for a regular OPA [Equations (2.34)–(2.36)] in terms of the variables u_1, u_2, and u_3. After transforming the OPA solutions [Equations (2.46)–(2.48)] in terms of u_1, u_2, and u_3 back to the original class-A variables a_1, a_2, and a_3, the evolution of the field amplitudes can be expressed as

$$a_1(z) = \sqrt{\frac{C_1}{(1 - \beta^2)(1 + \beta^2)}} \, \text{cn}(Z_a|m_a) \tag{4.4}$$

$$a_2(z) = \sqrt{\frac{C_2}{1 + \beta^2}} \, \text{dn}(Z_a|m_a) \tag{4.5}$$

$$a_3(z) = \sqrt{\frac{C_1}{1 - \beta^2}} \, \text{sn}(Z_a|m_a) \tag{4.6}$$

$$a_6(z) = \beta a_1(z) \tag{4.7}$$

where

$$C_1 = (1 - \beta^2)(1 + \beta^2)a_1^2(z) + (1 - \beta^2)a_3^2(z) \tag{4.8}$$

$$C_2 = (1 + \beta^2)a_2^2(z) + (1 - \beta^2)a_3^2(z) \tag{4.9}$$

31

are the Manley-Rowe conserved quantities [Equations (2.37) and (2.38)] expressed in terms of the field amplitudes a_1, a_2, and a_3. Here, $m_a = C_1/C_2$ and Z_a is as defined in Equation (2.44).

If β is larger than unity, the parametric gain provided by the pump cannot compensate for the nonlinear SFG loss. In this case, the net gain experienced by the signal field is always less than or equal to unity, regardless of the values of κ_a and the input photon flux densities. Therefore, it is impossible for the SF-OPO to get above threshold.

4.1.2 Class-B solutions

In class-B SF-OPO's, the OPO signal (pump) and the SFG lower (higher) frequency input fields have orthogonal polarizations. Therefore, the OPA and SFG processes are independent of each other in a single pass through the crystal. However, an intracavity polarization rotation of the signal field and an extracavity polarization rotation of the pump field with the use of half-wave retarders can couple the two processes and allow SFG to take place. The single-pass solutions are given by Equations (2.46)–(2.48) and (2.56)–(2.58).

4.1.3 Class-C solutions

The phase matching geometry for class-C SF-OPO's requires the polarizations of the OPO pump and the higher frequency SFG input fields to be orthogonal. The higher frequency SFG input field is provided by a polarization rotation of the pump, before the pump enters the cavity. In calculating the single-pass solutions, we take the total pump field amplitude to be a_p. We then rotate the polarization of this input field by and angle α_p so that the input OPO pump field amplitude is $a_3(0) = a_p \cos \alpha_p$, and the rotated pump (higher frequency SFG input) field amplitude is $a_5(0) = a_p \sin \alpha_p$.

Since analytical solutions of class-C coupled mode equations (3.5)–(3.9) are not available, we used the Runge-Kutta-Fehlberg method to calculate the evolution of the photon flux densities and the net signal gain. Figure 4.1 shows an example for the single-pass solutions of class-C coupled mode equations. For this example, we have taken $\alpha_p = 30°$, $\beta = 1.5$, and $a_2^2(0) = 0.3a_p^2$. The photon flux densities evolve periodically with a period of 10 in this example and the maximum value for the sum-frequency photon flux density is limited by the input rotated

Figure 4.1: Single-pass solutions for a class-C SF-OPA for $\beta = 1.5$. The evolution of the pump (p), signal (s), idler (i), polarization rotated pump (rp), and sum-frequency (sf) photon flux densities are shown as functions of the normalized propagation distance $\xi = \kappa_a a_p z$. All photon flux densities are normalized to the total input pump photon flux density a_p^2. For this example, $\alpha_p = 40°$, $\beta = 1.5$, and $a_2^2(0) = 0.3 a_p^2$.

pump photon flux density.

While calculating the single-pass solutions, we found that the field amplitudes oscillate either periodically or aperiodically as a function of z, depending on the initial field amplitudes and β. This behavior can best be analyzed by transforming the coupled mode equations (3.5)–(3.9) to a single differential equation similar to Equation (2.42). To do this, we use the class-C Manley-Rowe conserved quantities

$$C_1 = a_1^2(z) + a_3^2(z) = a_3^2(0) \tag{4.10}$$

$$C_2 = a_2^2(z) + a_3^2(z) + a_6^2(z) = a_2^2(0) + a_3^2(0) \tag{4.11}$$

$$C_3 = a_5^2(z) + a_6^2(z) = a_5^2(0) \tag{4.12}$$

and define new variables $\theta(z)$ and $\gamma(z)$ through

$$a_1(z) = \sqrt{C_1} \sin \theta(z) \tag{4.13}$$

$$a_3(z) = \sqrt{C_1} \cos \theta(z) \tag{4.14}$$

$$a_5(z) = \sqrt{C_3} \cos \gamma(z) \tag{4.15}$$

$$a_6(z) = \sqrt{C_3} \sin \gamma(z). \tag{4.16}$$

Since no idler or sum-frequency is present at the crystal input, $\theta(0)$ and $\gamma(0)$ are equal to an integer multiple of 2π; for convenience, we choose $\theta(0) = \gamma(0) = 0$. Substituting into Equations (3.5) and (3.9), we obtain

$$a_2(z) = \frac{1}{\kappa_a}\frac{d\theta}{dz} = \frac{1}{\kappa_b}\frac{d\gamma}{dz}. \tag{4.17}$$

When integrated this equation yields $\theta(z)/\kappa_a - \gamma(z)/\kappa_b = 0$, from which we obtain $\gamma(z) = \beta\theta(z)$. This relation, along with the Manley-Rowe relation for C_2, allows us to reduce the set of coupled mode equations to a single differential equation

$$\frac{1}{\kappa_a^2}\left(\frac{d\theta}{dz}\right)^2 + C_1\cos^2\theta + C_3\sin^2(\beta\theta) = C_2 \tag{4.18}$$

in the variable $\theta(z)$. The solution $\theta(z)$ either oscillates periodically around zero or increases monotonically, depending on the values of the Manley-Rowe quantities and β. If $C_1\cos^2\theta + C_3\sin^2(\beta\theta)$ is larger than C_2 for any value of θ, the field amplitudes oscillate periodically. In this case, the signal field is fully depleted inside the crystal, with the depletion locations coinciding with the maxima and minima of $\theta(z)$. If β has a rational value, there exists a θ value such that $\cos^2\theta = \sin^2(\beta\theta) = 1$. Then, the condition $C_1\cos^2\theta + C_3\sin^2(\beta\theta) > C_2$ is equivalent to $a_2^2(0) < a_5^2(0)$.

In the other case where $\theta(z)$ increases monotonically, the field amplitudes are periodic functions of z only if β has a rational value. Otherwise, $C_1\cos^2\theta + C_3\sin^2(\beta\theta)$ is an aperiodic function of θ, and the field amplitudes vary aperiodically.

Although Equation (4.18) gives more insight into the qualitative behavior of the solutions, in calculating the single-pass solutions we prefer to solve Equations (3.5)–(3.9) directly. The first term of Equation (4.18) brings about an ambiguity in the sign of $d\theta/dz$, and every time the signal field is depleted the corresponding sign change in $d\theta/dz$ needs to be taken care of in numerical solutions.

4.1.4 Class-D solutions

In class-D SF-OPO's, the polarizations of the OPO signal and the lower frequency SFG input are orthogonal. The lower frequency SFG input (rotated signal) is provided by an intracavity polarization rotation of the signal. In calculating the single-pass solutions, we take the total signal field amplitude to be a_s. We then
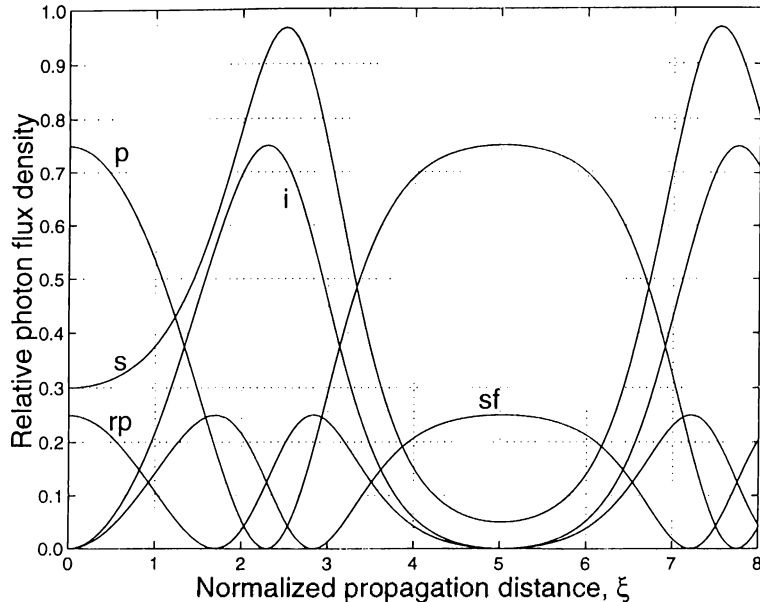
Figure 4.2: Single-pass solutions for a class-D SF-OPA for $\beta = 1.5$. The evolution of the pump (p), signal (s), idler (i), polarization rotated signal (rs), and sum-frequency (sf) photon flux densities are shown as functions of the normalized propagation distance $\xi = \kappa_a a_3(0)z$. All photon flux densities are normalized to $a_3^2(0)$. For this example, $\alpha_s = 40°$, $\beta = 1.5$, and the total input signal flux is $a_s^2 = 0.4 a_3^2(0)$.

rotate the polarization of this input field by an angle α_s so that the input OPO signal field amplitude is $a_2(0) = a_s \cos \alpha_s$, and the rotated signal (lower frequency SFG input) field amplitude is $a_4(0) = a_s \sin \alpha_s$.

We used the Runge-Kutta-Fehlberg method for the calculation of the class-D single-pass solutions as well. Figure 4.2 shows an example for the evolution of the photon flux densities in a class-D SF-OPA. We found that the photon flux densities oscillate periodically as functions of z, regardless of the values of the Manley-Rowe quantities and β. This behavior is easier to analyze if the coupled mode equations are reduced to a single differential equation similar to Equation (4.18). Furthermore, this differential equation can be used to obtain conditions that maximize conversion efficiency, as outlined in Chapter 5.

The Manley-Rowe conserved quantities for class-D SF-OPO's are

$$ C_1 = a_2^2(z) - a_1^2(z) = a_2^2(0) \tag{4.19} $$

$$ C_2 = a_2^2(z) + a_3^2(z) + a_6^2(z) = a_2^2(0) + a_3^2(0) \tag{4.20} $$

$$ C_3 = a_4^2(z) + a_6^2(z) = a_4^2(0) . \tag{4.21} $$

35

We define new variables $\theta(z)$ and $\gamma(z)$ through

$$a_1(z) = \sqrt{C_1} \sinh \theta(z) \tag{4.22}$$

$$a_2(z) = \sqrt{C_1} \cosh \theta(z) \tag{4.23}$$

$$a_4(z) = \sqrt{C_3} \cos \gamma(z) \tag{4.24}$$

$$a_6(z) = \sqrt{C_3} \sin \gamma(z). \tag{4.25}$$

Since $a_1(0) = a_6(0) = 0$, $\theta(0) = 0$ and $\gamma(0)$ is an integer multiple of 2π; we choose $\gamma(0) = 0$ for convenience. When these transformations are substituted into the coupled mode equations (3.10) and (3.14), the pump field amplitude is obtained in terms of $\theta(z)$ or $\gamma(z)$ as

$$a_3(z) = \frac{1}{\kappa_a} \frac{d\theta}{dz} = \frac{1}{\kappa_b} \frac{d\gamma}{dz}. \tag{4.26}$$

It is then possible to integrate this equation and get a fourth conserved quantity $C_1 = \theta(z)/\kappa_a - \gamma(z)/\kappa_b = 0$. Using this relation and the Manley-Rowe relation for C_2, we obtain a single differential equation

$$\frac{1}{\kappa_a^2} \left(\frac{d\theta}{dz} \right)^2 + C_1 \cosh^2 \theta + C_3 \sin^2(\beta\theta) = C_2 \tag{4.27}$$

in the variable $\theta(z)$. As $\theta(z)$ starts from zero at the crystal input and increases, the second term in Equation (4.27) increases monotonically until $d\theta/dz$ becomes zero. We observe from Equation (4.26) that this point corresponds to complete pump depletion. Since the first term of Equation (4.27) cannot be negative, $\theta(z)$ has to decrease from this point on. Hence, $\theta(z)$ oscillates periodically around zero, and the field amplitudes also evolve periodically with the period being identified by complete pump depletion. As in class-C single-pass solutions. we prefer to solve the original coupled mode equations [Equations (3.10)–(3.14)] in computing the single-pass signal gain.

4.2   Single-pass solutions of SD-OPO's

Of the three SD-OPO classes, analytical solutions are readily available only for class-B coupled mode equations. For this class, the OPA and SHG processes are not coupled in the crystal and analytical solutions for the two processes can be used separately. For class-A and class-C SD-OPO's, we used the Runge-Kutta-Fehlberg method to solve the coupled mode equations and to compute the single-pass parametric gain.
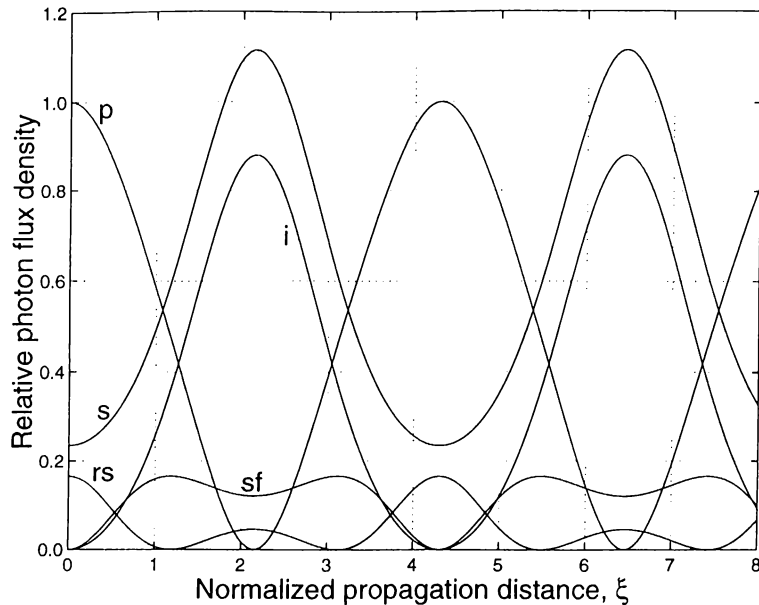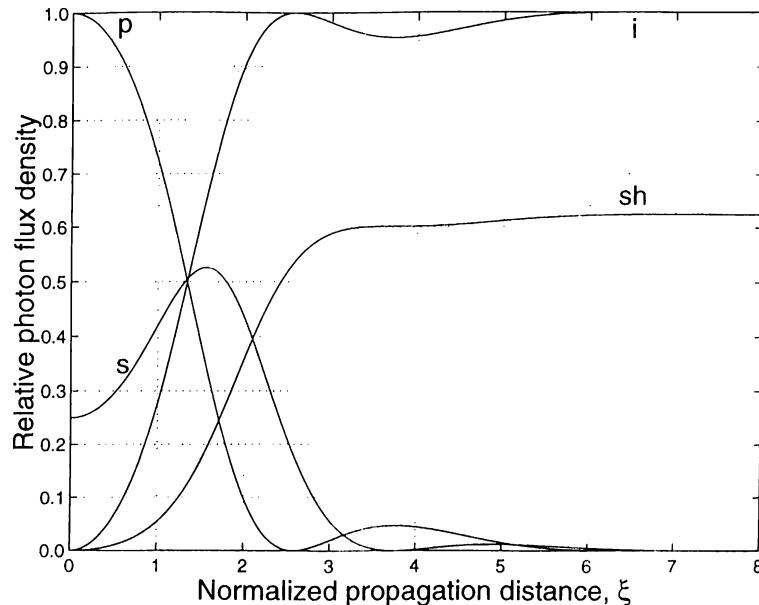
Figure 4.3: Single-pass solutions for a class-A SD-OPA for $\beta = 1.5$. The evolution of the pump (p), signal (s), idler (i), and second-harmonic (sh) photon flux densities are shown as functions of the normalized propagation distance ξ. All photon flux densities are normalized to the input pump photon flux density and $a_2^2(0) = 0.25a_3^2(0)$.

4.2.1 Class-A solutions

Figure 4.3 shows an example for the evolution of the photon flux densities in a class-A SD-OPA. The normalized propagation distance is defined to be $\xi = \kappa_a a_3(0)z$, as in OPA's, and all photon flux densities are normalized to the input pump photon flux density. For this example, β is taken to be 1.5.

At the beginning of the interaction, the OPA process is dominant and the signal photon flux density increases with increasing ξ. However, the nonlinear loss due to the increasing second-harmonic eventually overcomes the parametric gain and the signal flux density begins to decrease after $\xi = 1.6$. The pump field is completely depleted at $\xi = 2.5$, and back-conversion of the signal and the idler to the pump begins after this point. However, the amount of back-conversion is small, since much of the signal flux density is already converted to the second-harmonic. At $\xi = 7$, essentially the entire pump and the signal is converted to the second-harmonic, and the interaction stops. Throughout the interaction, the oscillatory nature of the OPA process is dampened by the conversion of the signal to the second-harmonic, and the class-A single-pass solutions are not periodic.

The parameter β is a measure of the relative strengths of the OPA and SHG

processes. With increasing β, the SHG process becomes more prominent, the oscillatory behavior due to the OPA process decreases in amplitude, and conversion to the second-harmonic is completed earlier in the crystal.

There are only two Manley-Rowe conserved quantities in class-A interactions. These quantities are

$$C_1 = a_1^2(z) + a_3^2(z) = a_3^2(0) \tag{4.28}$$

$$C_2 = a_2^2(z) + a_3^2(z) + 2a_6^2(z) = a_2^2(0) + a_3^2(0). \tag{4.29}$$

4.2.2 Class-B solutions

In class-B SD-OPO's, the OPO signal and the SHG fundamental have orthogonal polarizations, and the OPA and SHG processes are independent of each other in a single-pass through the crystal. However, an intracavity polarization rotation of the signal field with the use of a half-wave retarder can couple the two processes and allow frequency doubling to take place. The single-pass solutions are given by Equations (2.46)–(2.48) and (2.66)–(2.67).

4.2.3 Class-C solutions

Since class-C self-doubling and SF-OPO's are governed by the same coupled mode equations [Equations (3.19)–(3.23) and (3.5)–(3.9)], the single-pass solutions exhibit the same behavior. In both cases, the coupling in the crystal is through the signal field. However, the second fundamental component a_5 in class-C SD-OPO's is provided by intracavity polarization rotation of the signal field, whereas the higher frequency SFG input a_5 in class-C SF-OPO's is provided by extracavity polarization rotation of the pump. The class-C SD-OPO performance therefore has a different dependence on the design parameters, as shown in Chapter 5.

Chapter 5

Plane-Wave Theory of Single-Crystal Upconversion OPO's

A singly-resonant single-crystal upconversion OPO is constructed by placing the nonlinear crystal inside a resonator that provides feedback at the signal frequency. In contrast with regular OPO's, output coupling for the signal field is not necessary, since the useful light output is either the frequency-doubled signal field or the sum-frequency of the signal and the pump. However, the cavity will inevitably have a few percent of linear loss (L) at the signal frequency, due to less than unity reflectances of the resonator mirrors and imperfect antireflection coatings on the nonlinear crystal. This linear loss can be represented by a lumped cavity reflectance $R_L = 1 - L$.

In single-crystal upconversion OPO's, the saturation of parametric gain is completely characterized by the nonlinear drive D, the ratio of the coupling coefficients $\beta = \kappa_b/\kappa_a$, and the polarization rotation angle (if any) [29], [30]. The nonlinear drive for single-crystal upconversion OPO's is defined as $D = (\kappa_a a_p l)^2$, where a_p^2 is the pump photon flux density at the crystal input. For class-B and class-C SF-OPO's, $a_p^2 = a_3^2(0) + a_5^2(0)$ is the total pump photon flux density before polarization rotation of the pump field, whereas in other upconversion OPO's there is no pump polarization rotation and $a_p^2 = a_3^2(0)$.

As in regular OPO's, if the small-signal gain is larger than the resonator loss, oscillation starts. The initial signal photon flux provided by parametric

fluorescence grows until the upconversion OPO reaches steady-state. In steady-state, the parametric gain in the nonlinear crystal exactly compensates for the resonator loss and this condition is expressed as

$$R_L g[a_2^2(0)] = 1 \qquad (5.1)$$

where $g = a_2^2(l)/a_2^2(0)$ is the single-pass saturated gain for the signal field. The intracavity signal photon flux density in steady-state $a_2^2(0)$ can in general be found by solving Equation (5.1) iteratively using the single-pass solutions outlined in Chapter 4. In doing this, we used the secant method for numerical root-finding.

The performance of the secant method depends on the initial approximations provided. When investigating the behavior of single-crystal upconversion OPO's, we usually vary one of the parameters that influence gain saturation while the remaining parameters are kept constant. In such cases, the solution $a_2^2(0)$ from the latest parameter value is a very good initial approximation for the solution corresponding to the next parameter value. With this choice for the initial approximation, the secant method typically takes five to fifteen iterations to converge to the solution within a relative tolerance of 10^{-8}.

Once the intracavity signal photon flux density is known, all other fields at the crystal output can be calculated using single-pass solutions. From the output photon flux densities, photon conversion efficiency and pump depletion can be calculated as measures of performance for single-crystal upconversion OPO's. The photon conversion efficiency for upconversion OPO's is defined as the ratio of twice the output upconverted flux density to the input pump flux density, $\eta = 2a_6^2(l)/a_3^2(0)$, since two pump photons are needed for one upconverted photon. The conversion efficiency represents the overall efficiency of the two-step process from the pump to the signal and then to either the sum-frequency or the doubled signal, and is equal to unity for total conversion.

In regular OPO's, pump depletion $[1 - a_3^2(l)/a_3^2(0)]$ is an alternative measure of performance, since maximum conversion requires complete pump depletion. As shown in this chapter, this is no longer the case in single-crystal upconversion OPO's, except for class-A and class-D SF-OPO's.

In general, Equation (5.1) may have more than one solution. In this thesis, we investigate the steady-state performance of single-crystal upconversion OPO's, and always choose the smallest of these solutions, assuming that the intracavity signal field builds up from noise to reach this smallest solution. However, the dynamical evolution of the signal field as it builds up from noise can also be

simulated [30], [40], by starting with parametric fluorescence and iterating the single-pass solutions several times, multiplying the signal flux density by R_L after each pass through the crystal. This analysis has revealed that both SF-OPO's and SD-OPO's may display periodic or chaotic oscillations at high values of the nonlinear drive. Furthermore, if the nonlinear drive is high enough, the SF-OPO may reach different steady-state solutions depending on the initial signal flux density. It has been found that these steady-state solutions are stable and the SF-OPO thus exhibits multistability [30].

5.1 SF-OPO's

5.1.1 Class-A SF-OPO's

As pointed out in Chapter 4, class-A SF-OPO's can get above threshold only if β is less than unity. Under this condition, the small-signal gain is

$$g_0 = \cosh^2 \sqrt{(1 - \beta^2)D}. \tag{5.2}$$

The threshold nonlinear drive D_{th} is found by solving $R_L g_0 = 1$ for D. Since g_0 depends on β, D_{th} is influenced by the presence of the SFG process. This is in contrast with SD-OPO's.

Conversion efficiency is maximized if the pump field is fully depleted at the crystal output, as shown by the Manley-Rowe relation (4.8) and Equation (4.7). To obtain the nonlinear drive for complete pump depletion, we first evaluate the Manley-Rowe relation (4.9) at $z = 0$ and $z = l$ and use the steady-state oscillation condition [Equation (5.1)], to get the intracavity signal flux density normalized to the input pump flux density

$$\frac{a_2^2(0)}{a_3^2(0)} = \frac{(1 - L)(1 - \beta^2)}{L(1 + \beta^2)}. \tag{5.3}$$

Using Equation (5.3), we find that $m_a = L$. The pump field amplitude has a $\mathrm{sn}(Z|m)$ functional dependence which assumes its zeros at even multiples of the Jacobi quarter-period K. Therefore, complete pump depletion at $z = l$ requires that

$$K - \kappa_a \sqrt{C_2}\, l = -2nK \qquad n = 0, 1, 2, \ldots \tag{5.4}$$

This relation leads to a family of optimum nonlinear drive values

$$D_{opt} = \frac{L}{1 - \beta^2} \left[(2n + 1)K\right]^2 \tag{5.5}$$

41

that maximizes the conversion efficiency for given values of β and L. The ratio D_{opt}/D_{th} depends only on L, similar to a regular OPO [10]. Only the smallest D_{opt} (corresponding to $n = 0$) is of interest, since for $n > 0$ Equation (5.3) does not yield the smallest solution of equation (5.1).

Figure 5.1 shows the conversion efficiency as a function of the nonlinear drive for various β values at a constant $L = 0.04$. The peak of each curve is at D_{opt} with a value of

$$\eta_{max} = \frac{2\beta^2}{1 + \beta^2}. \tag{5.6}$$

This value is a function of β only. As β increases towards unity, η_{max} approaches unity, while D_{opt} and D_{th} increase without bound.
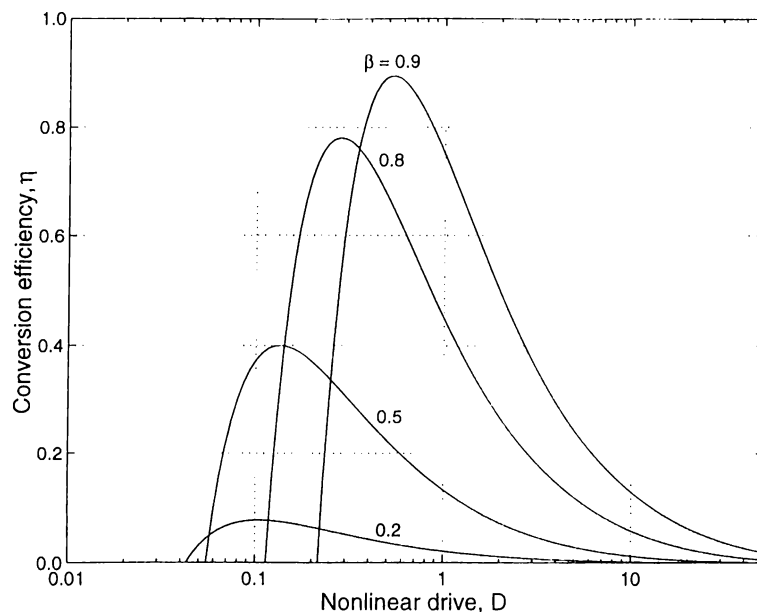
Figure 5.1: Conversion efficiency of class-A SF-OPO's as a function of the nonlinear drive for various values of β. For each case, $L = 0.04$.

The cavity loss L at the signal frequency results in the loss of signal photons from the cavity. One would expect that this useless loss should be minimized for maximum conversion to the sum-frequency. However, as illustrated in Figure 5.2, the cavity loss can be adjusted to maximize the conversion efficiency. At a constant β value of 0.8, the conversion efficiency curve shifts to the right with increasing cavity loss, whereas the peak conversion efficiency does not change, in agreement with the analytical result given in Equation (5.6). At a nonlinear drive of unity, a relatively large cavity loss of $L = 0.14$ is needed for maximum ($\eta = 0.78$) conversion.

42
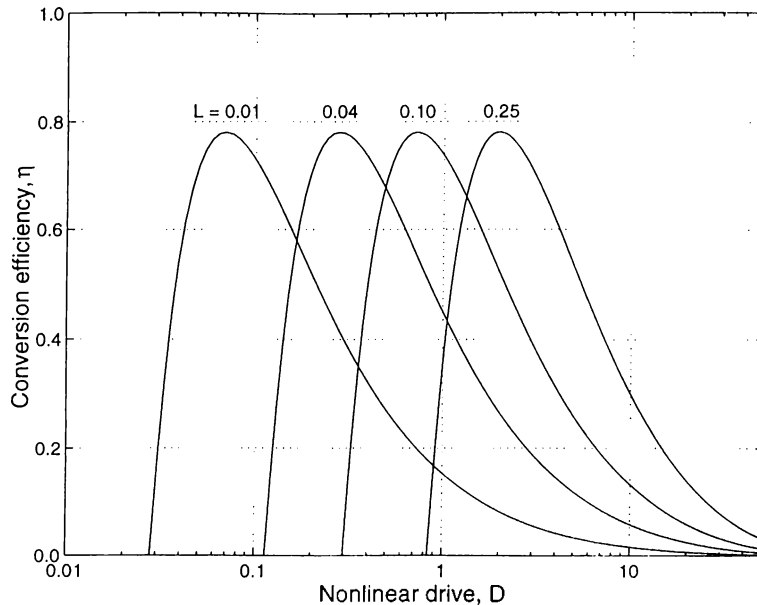
Figure 5.2: Conversion efficiency as a function of the nonlinear drive for various values of L for a class-A SF-OPO. For each case, $\beta = 0.8$.

5.1.2 Class-B SF-OPO's

Class-B SF-OPO's require an intracavity polarization rotation for the signal field and an extracavity polarization rotation for the pump field. Two different modes of operation are possible, depending on the polarization rotation configuration employed for the signal field. In the first case, the signal polarization is rotated by an amount $\alpha_s < 90°$, so that a $\sin^2 \alpha_s$ fraction of the OPO signal flux is coupled to the lower frequency SFG input field $a_4(0)$, while the remaining $\cos^2 \alpha_s$ fraction becomes the input signal $a_2(0)$. At each pass through the crystal, the OPO signal a_2 experiences parametric gain, whereas the rotated signal a_4 is depleted due to SFG. Here, we assume that the residual rotated signal at the crystal output $a_4(l)$ is either coupled out of the cavity with the use of a polarizing beamsplitter, or negligible due to strong conversion. If instead both the signal and the rotated signal are resonated, the polarization mixing at the retarder will result in the interference of the two fields in an uncontrolled fashion.

In this configuration, the OPO signal experiences a linear loss of $\sin^2 \alpha_s$ in addition to other resonator losses and the total resonator reflectance becomes $R_L \cos^2 \alpha_s$. There is no nonlinear output coupling in this situation; the intracavity signal flux is not affected by the presence of the SFG process. Even though the SFG process is internal to the OPO resonator, it does not benefit from high values of the intracavity signal flux density. As such, this configuration is not expected

43

to be particularly efficient.

On the other hand, a different mode of operation is achieved if the residual rotated signal $a_4(l)$ is not coupled out and α_s is set to 90°. In this configuration, the retarder switches around the polarizations of the OPO signal $a_2(l)$ and the residual rotated signal $a_4(l)$ with no resulting interference due to polarization mixing. The OPO signal at the crystal output provides the rotated signal $a_4(0)$ for the next round trip, whereas the residual rotated signal becomes the OPA input $a_2(0)$. As in the previous configuration, the polarization of the pump field is rotated before entering the cavity to provide the higher frequency SFG input field $a_5(0)$.

The distribution of the pump photon flux density between the two processes can be optimized by adjusting the pump polarization rotation angle α_p. Figure 5.3 shows the conversion efficiency and the depletion of the pump and the rotated pump flux densities as functions of α_p for four different values of β. In all cases, the nonlinear drive is kept constant at unity and $L = 0.04$. For $\beta = 0.7$ in Figure 5.3(a), a maximum conversion efficiency of 0.71 is achieved at $\alpha_p = 41°$, whereas the pump and the rotated pump are fully depleted at $\alpha_p = 42°$ and $\alpha_p = 17°$, respectively. The SF-OPO is below threshold for $\alpha_p \geq 51°$.
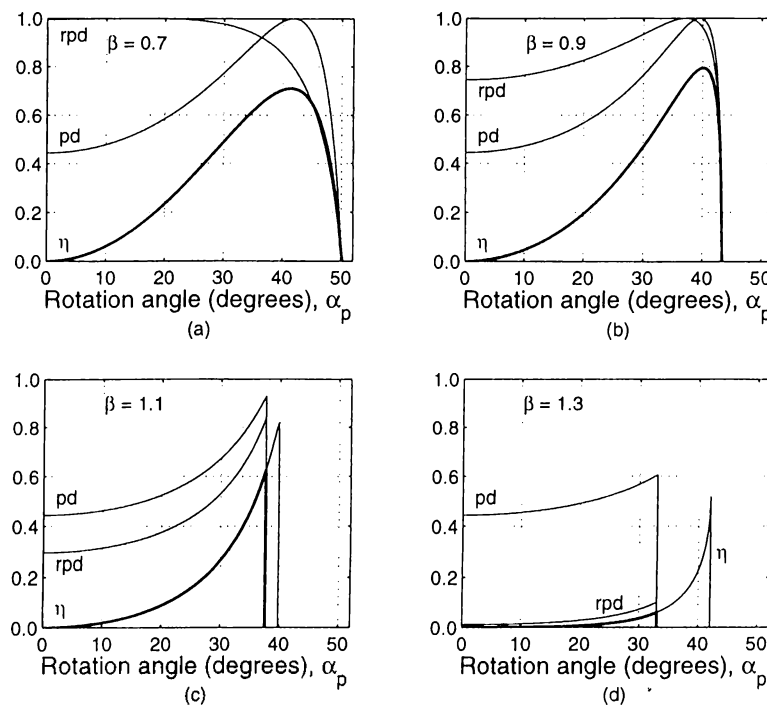

Figure 5.3: Conversion efficiency (η), pump depletion (pd), and rotated pump depletion (rpd) as functions of the pump polarization rotation angle for a class-B SF-OPO. The nonlinear drive is unity and $L = 0.04$ in all cases.

Figure 5.3(b) with a larger β of 0.9 shows a similar behavior with a higher conversion efficiency of 0.79. The SF-OPO gets below threshold at an earlier value of $\alpha_p = 44°$, since the SFG process is stronger in this case. For larger values of β, the maximum conversion efficiency increases up to a value of 0.81 and then begins to decrease as a result of the threshold α_p being smaller than the optimum α_p. Figure 5.3(c) and (d) show two examples of this situation. Here, the SF-OPO achieves its maximum conversion efficiency right before going below threshold. This behavior is related to the unusual saturation characteristics of the parametric gain; starting from g_0 at $a_2^2(0) = 0$, $g[a_2^2(0)]$ first increases with increasing $a_2^2(0)$, and then decreases to cross the loss line $1/R_L$ at the intracavity signal flux density $a_2^2(0) = x$. When α_p is increased, g_0 decreases and becomes less than $1/R_L$. If the SF-OPO is turned on at this point, oscillations cannot build up in the cavity. However, if one increases α_p while the SF-OPO is oscillating at $a_2^2(0) = x$, the oscillations continue past the threshold α_p value, as shown in Figure 5.3(c) and (d).

Both the threshold α_p and the threshold nonlinear drive can be found by solving $R_L g_0 = 1$. Since the OPO and the SFG processes are independent in a single-pass through the crystal and the retarder switches around the polarizations of a_2 and a_4 in each round trip, the signal field has to be followed for two cavity round trips to find the threshold condition. The small-signal gain over two round trips can be expressed as

$$g_0 = R_L \cosh^2\left(\sqrt{D} \cos\alpha_p\right) \cos^2\left(\beta\sqrt{D} \sin\alpha_p\right). \qquad (5.7)$$

where the $\cosh^2(\sqrt{D} \cos\alpha_p)$ factor represents the gain of the OPO signal in the first pass through the crystal, whereas the $\cos^2(\beta\sqrt{D} \sin\alpha_p)$ factor represents the loss due to SFG in the second pass. The oscillatory nature of the $\cos^2(\beta\sqrt{D} \sin\alpha_p)$ factor in Equation (5.7) results in a number of ranges for the nonlinear drive where the SF-OPO is below threshold. Figure 5.4 shows the dependence of the conversion efficiency on the nonlinear drive for four different values of β. In each case, α_p is adjusted to maximize the conversion efficiency at unity nonlinear drive. We observe a number of sub-threshold regions in Figure 5.4.
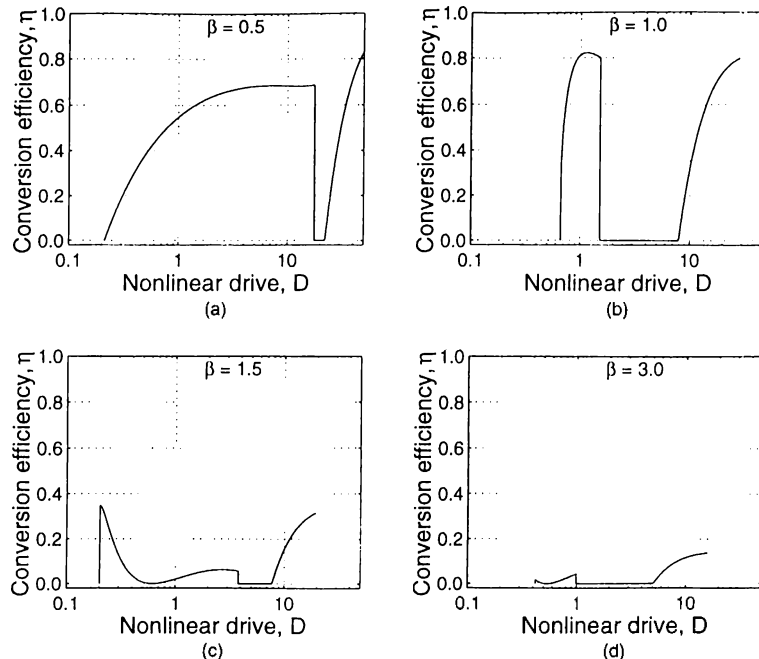
Figure 5.4: Conversion efficiency as a function of the nonlinear drive for different values of β for a class-B SF-OPO. For each β value, the pump polarization rotation angle α_p is adjusted to maximize the conversion efficiency at a nonlinear drive of unity. (a) $\beta = 0.5$, $\alpha_p = 44.1°$; (b) $\beta = 1.0$, $\alpha_p = 39.9°$; (c) $\beta = 1.5$, $\alpha_p = 24.6°$; (d) $\beta = 3.0$, $\alpha_p = 15.54°$. For each case, $L = 0.04$.

5.1.3 Class-C SF-OPO's

The phase matching geometry of class-C SF-OPO's leads to orthogonal polarizations for the OPO pump and the higher frequency SFG input fields. A half-wave retarder provides adjustable rotation of the pump polarization before the pump beam enters the cavity. For a polarization rotation angle of α_p, a $\sin^2 \alpha_p$ fraction of the total input pump flux density a_p^2 is used as the higher frequency SFG input $a_5^2(0)$, whereas the remaining pump flux density $a_3^2(0)$ provides parametric gain for the signal field. With this configuration, the distribution of the pump photon flux density between the two processes can be adjusted to maximize the conversion efficiency.

Figure 5.5 shows the conversion efficiency and the depletion of the pump and the rotated pump (higher frequency SFG input) flux densities as functions of the polarization rotation angle α_p for four different values of β, where the nonlinear drive is kept constant at unity and $L = 0.04$. For $\beta = 0.5$ in Figure 5.5(a), a maximum conversion efficiency of 0.64 is achieved at $\alpha_p = 46°$, whereas the pump is fully depleted at $\alpha_p = 51°$. The depletion of the rotated pump starts at

46
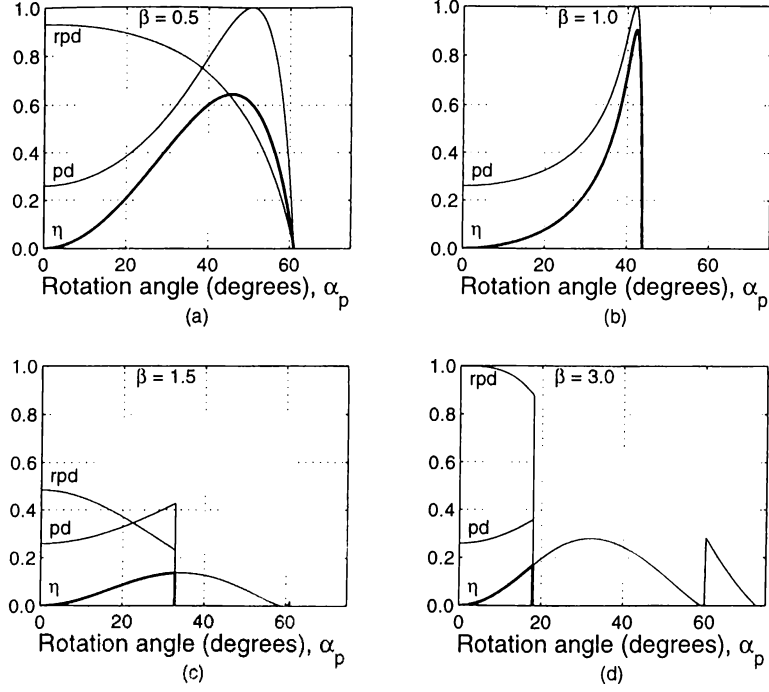
Figure 5.5: Conversion efficiency (η), pump depletion (pd), and rotated pump depletion (rpd) as functions of the pump polarization rotation angle for a class-C SF-OPO. The nonlinear drive is unity and $L = 0.04$ in all cases.

0.93 with α_p just above zero and decreases monotonically until the SF-OPO gets below threshold at $\alpha_p = 62°$.

For $\beta = 1$ in Figure 5.5(b), the maximum conversion efficiency is higher (0.90), and complete pump depletion coincides with maximum conversion. For this particular value of β, the depletion of the pump and the rotated pump fields are equal for all values of α_p and D, since $\gamma(z) = \theta(z)$ for $\beta = 1$. However, simultaneous depletion of both pump components is possible only when β or $1/\beta$ is an odd integer, since $\cos(\beta\theta)$ and $\cos\theta$ can become equal to zero at the same θ value only then.

For β larger than unity, the conversion efficiency achieves its maximum right before the threshold α_p, similar to class-B SF-OPO's. Figure 5.5(c) and (d) show examples of this behavior for $\beta = 1.5$ and 3, respectively. Note that a solution of the steady-state oscillation condition [Equation (5.1)] may exist beyond the threshold α_p, even though the intracavity signal cannot build up from noise to reach this solution.

Both the threshold nonlinear drive and the threshold α_p can be found by
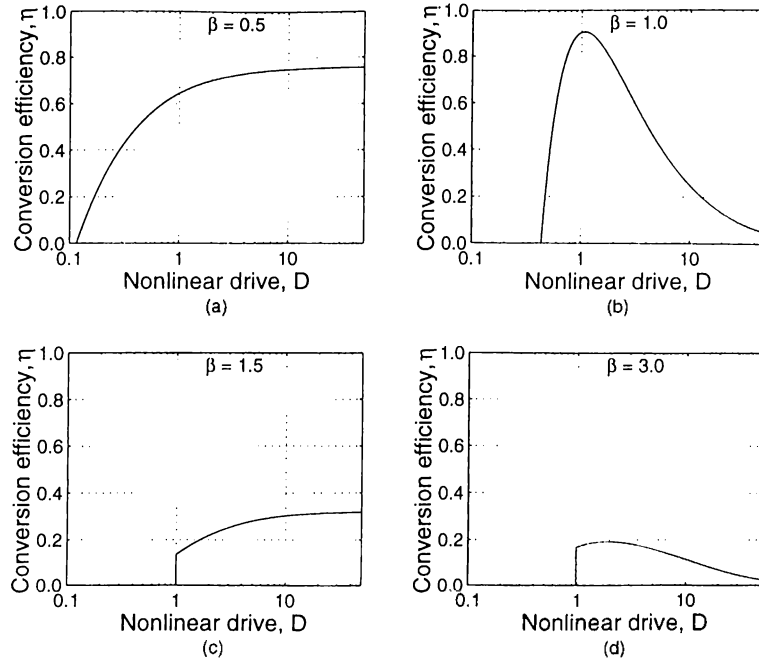
Figure 5.6: Conversion efficiency as a function of the nonlinear drive for different values of β for a class-C SF-OPO. For each β value, the pump polarization rotation angle α_p is adjusted to maximize the conversion efficiency at a nonlinear drive of unity. (a) $\beta = 0.5$, $\alpha_p = 45.9°$; (b) $\beta = 1.0$, $\alpha_p = 42.3°$; (c) $\beta = 1.5$, $\alpha_p = 32.9°$; (d) $\beta = 3.0$, $\alpha_p = 18.03°$. For each case, $L = 0.04$.

equating the small-signal gain

$$ g_0 = \cosh^2 \left(\cos \alpha_p \sqrt{(1 - \beta^2 \tan^2 \alpha_p)D} \right). \tag{5.8} $$

to $1/R_\mathrm{L}$. Note that Equation (5.8) is valid only if $\beta \tan \alpha_p \leq 1$, otherwise $g_0 < 1$.

Figure 5.6 shows the dependence of the conversion efficiency on the nonlinear drive for four different values of β. For each case, α_p is adjusted to maximize η at $D = 1$. We observe that the maximum conversion efficiency for $\beta = 0.5$ and $\beta = 1$ is higher than the maximum values for $\beta = 1.5$ and $\beta = 3$.

5.1.4 Class-D SF-OPO's

In class-D SF-OPO's, the polarizations of the OPO signal a_2 and the lower frequency SFG input a_4 are orthogonal. An intracavity half-wave retarder provides the SFG input $a_4(0)$ by rotating the signal polarization. There are two modes of operation, as in class-B SF-OPO's, depending on the signal polarization rotation angle α_s.

For the configuration where $0° < \alpha_s < 90°$, we assume that the rotated signal field (lower frequency SFG input) at the output of the crystal is either coupled

48

out of the cavity with a polarizing beamsplitter or strongly depleted, so that interference due to polarization mixing at the half-wave retarder is avoided. In this configuration, maximum conversion to the sum-frequency takes place when both the pump and the rotated signal fields are fully depleted at the output. The nonlinear drive and α_s can be adjusted to deplete these two fields completely and maximize η.

The depletion of the rotated signal does not depend on the value of the nonlinear drive. To arrive at this conclusion, we first note that $R_{\mathrm{L}} a_2^2(l) = a_2^2(0) + a_4^2(0)$, and obtain

$$\frac{a_2^2(l)}{a_2^2(0)} = \cosh^2 \theta(l) = \frac{1 + \tan^2 \alpha_s}{R_{\mathrm{L}}} \tag{5.9}$$

where $\theta(z)$ is the solution to Equation (4.27). Equation (5.9) shows that $\theta(l)$ depends only on α_s and R_{L}. The rotated signal depletion at the output is

$$1 - \frac{a_4^2(l)}{a_4^2(0)} = 1 - \cos^2(\beta \theta(l)) \tag{5.10}$$

and independent of the value of D.

For the rotated signal to be fully depleted, the product $\beta\theta(l)$ should be equal to an odd multiple of $\pi/2$. Since the $\beta\theta(l) = \pi/2$ case requires smaller values for D and α_s, we consider this case only. Using Equation (5.9), the angle α_s that depletes the rotated signal for given values of β and R_{L} is found to be

$$\alpha_s = \tan^{-1} \sqrt{R_{\mathrm{L}} \cosh^2(\pi/2\beta) - 1} \ . \tag{5.11}$$

Complete depletion of the pump takes place when the first term in Equation (4.27) representing the pump photon flux density is equal to zero. This condition allows us to obtain the ratio of C_1 and C_2 as

$$m = \frac{C_1}{C_2} = \frac{1}{\cosh^2 \theta + \tan^2 \alpha_s \, \sin^2(\beta\theta)}. \tag{5.12}$$

Equation (5.12) also determines the ratio of the intracavity signal flux density to the input pump flux density through the Manley-Rowe relations (4.19) and (4.20). In the case of simultaneous depletion of the pump and the rotated signal fields at the crystal output, Equation (5.12) can be expressed in terms of β and R_{L} as

$$m_{\mathrm{opt}} = \frac{1}{(R_{\mathrm{L}} + 1)\cosh^2(\pi/2\beta) - 1}. \tag{5.13}$$

We then integrate Equation (4.27) and obtain the optimum nonlinear drive as

$$D_{\mathrm{opt}} = (1 - m_{\mathrm{opt}}) \left[\int_0^{\pi/2\beta} [1 - m_{\mathrm{opt}}(\cosh^2 \phi + \tan^2 \alpha_s \, \sin^2(\beta\phi))]^{-1/2} d\phi \right]^2 \tag{5.14}$$
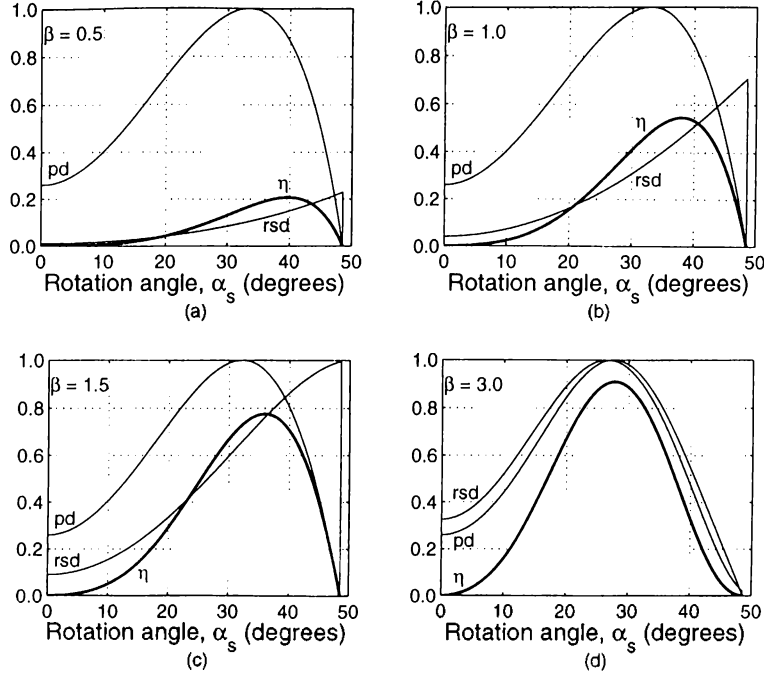
49

Figure 5.7: Conversion efficiency (η), pump depletion (pd), and rotated signal depletion (rsd) as functions of the signal polarization rotation angle for a class-D SF-OPO. The nonlinear drive is unity and $L = 0.04$ in all cases.

where α_s and m_{opt} are given by Equations (5.11) and (5.13), respectively. The integral in Equation (5.14) has an integrable singularity at its upper limit, and can be evaluated numerically after a change of variable $\phi = \pi/2\beta - \rho^2$ eliminates the singularity [41].

The optimum nonlinear drive D_{opt} decreases with increasing values of β. The maximum conversion efficiency achieved at D_{opt} is

$$\eta_{max} = 2\frac{R_L \cosh^2(\pi/2\beta) - 1}{(R_L + 1)\cosh^2(\pi/2\beta) - 2} . \tag{5.15}$$

For larger values of β, η_{max} decreases rapidly with increasing cavity losses.

Figure 5.7 shows η and the depletion of the pump and the rotated signal flux densities as functions of α_s for four different values of β, where D is kept constant at unity and $L = 0.04$. Note that as β gets larger, the peak conversion efficiency increases and shifts to smaller values of α_s. The threshold α_s is independent of β since the net small-signal gain $g_0 = \cos^2 \alpha_s \cosh^2 \sqrt{D}$, which includes the linear loss due to polarization rotation, does not depend on β. Figure 5.8 shows the dependence of η on D for four different values of β. For each β value, α_s is adjusted to maximize η at unity nonlinear drive. The peak conversion efficiency is largest in Figure 5.8(d), since D_{opt} is closer to unity for $\beta = 3$ than for the
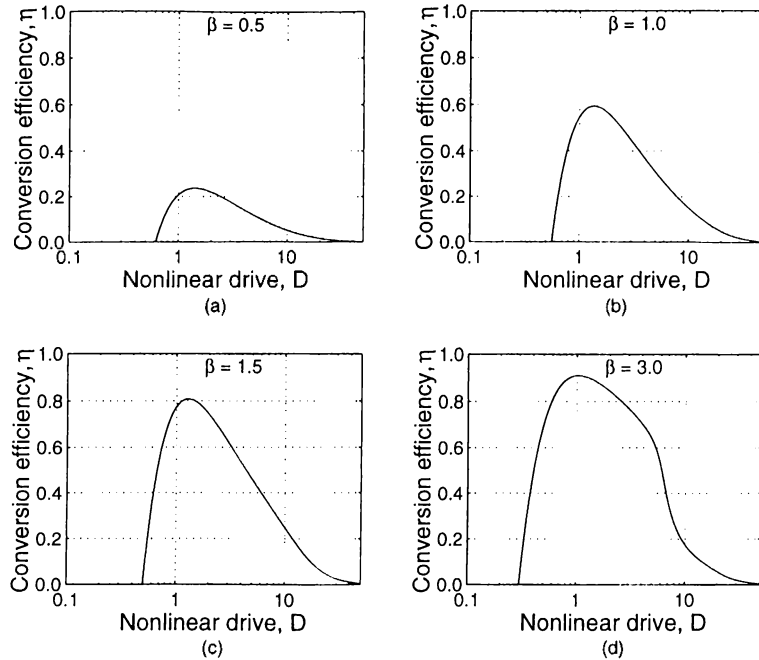
Figure 5.8: Conversion efficiency as a function of the nonlinear drive for various values of β for a class-D SF-OPO. For each β value, the signal polarization rotation angle α_s is adjusted to maximize the conversion efficiency at a nonlinear drive of unity. (a) $\alpha = 39.7°$, $\beta = 0.5$; (b) $\alpha = 38.1°$, $\beta = 1$; (c) $\alpha = 35.9°$, $\beta = 1.5$; (d) $\alpha = 27.8°$, $\beta = 3$. For each case, $L = 0.04$.

other β values.

If α_s is set to 90°, the retarder switches around the polarizations of the OPO signal $a_2(l)$ and the lower frequency SFG input $a_4(l)$ after each pass through the crystal. Since the OPO and the SFG processes are coupled in the crystal, iterating the single-pass solutions to simulate the intracavity build-up of the signal and the rotated signal flux densities is more appropriate for this configuration [30].

5.2 SD-OPO's

5.2.1 Class-A SD-OPO's

Figure 5.9 shows the photon conversion efficiency, pump depletion and intracavity signal flux density as functions of the nonlinear drive for four different values of β. The intracavity signal flux density is shown normalized to the input pump flux density. R_L is taken to be 0.96 in all cases. The threshold nonlinear drive D_{th} is independent of β. This is because conversion to the second-harmonic is negligible in the small-signal regime and the small-signal gain is not affected by
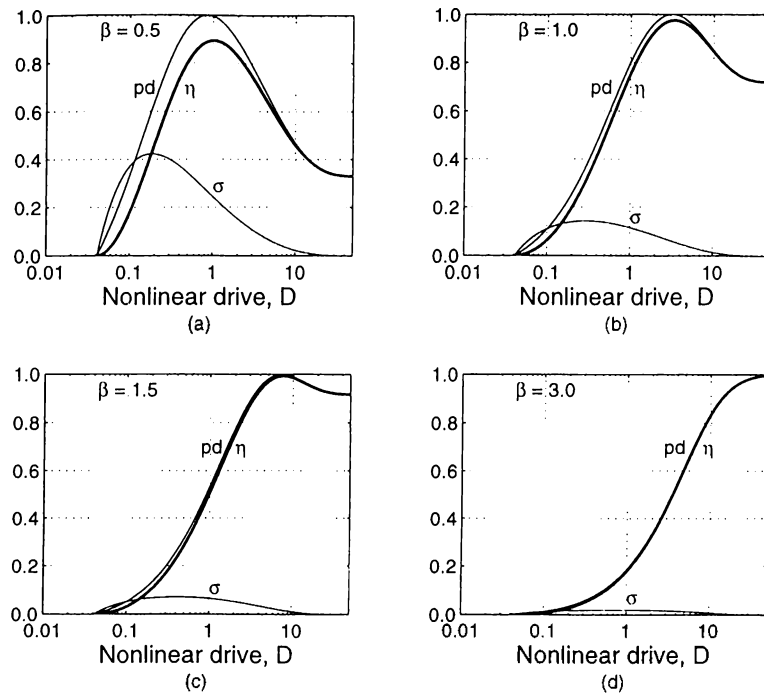
51

Figure 5.9: Conversion efficiency (η), pump depletion (pd), and intracavity signal flux density normalized to the input pump flux density (σ) as functions of the nonlinear drive for class-A SD-OPO's. R_L is taken to be 0.96 for (a) $\beta = 0.5$, (b) $\beta = 1.0$, (c) $\beta = 1.5$, and (d) $\beta = 3.0$.

the SHG process. Hence, the threshold nonlinear drive of 0.041 is equal to that of a regular OPO with $R = 0.96$.

In class-A SD-OPO's, maximum conversion does not coincide with complete pump depletion, but the conversion efficiency and pump depletion curves are very close. As β increases, the two quantities become nearly equal. The Manley-Rowe conserved quantity of Equation (4.29) can be used to formulate a relation between the photon conversion efficiency, pump depletion, and intracavity signal flux density (normalized to the input pump flux density). Evaluating Equation (4.29) at $z = l$ and $z = 0$, dividing both sides of the equality by the input pump flux density $a_3^2(0)$, and using the steady-state oscillation condition [Equation (5.1)], we obtain

$$\delta = \eta + \left(\frac{1}{R_L} - 1\right)\sigma \tag{5.16}$$

where δ is the pump depletion and $\sigma = a_2^2(0)/a_3^2(0)$ is the intracavity signal flux density normalized to the input pump flux density. Since no output coupling is employed, the resonator loss is usually small and the factor in front of σ is typically smaller than $1/10$. Hence, conversion efficiency and pump depletion are

nearly equal. As β increases, the intracavity signal flux decreases as a result of the nonlinear output coupling through the SHG process and the depletion and conversion curves begin to overlap.

We observe that maximum conversion efficiency is high for all values of β shown. As β increases, the nonlinear drive for maximum conversion increases and becomes more difficult to attain. However, variations from this optimum value do not affect the conversion efficiency significantly.

5.2.2   Class-B SD-OPO's

Class-B SD-OPO's require an intracavity polarization rotation for the signal field. Two different modes of operation are possible, depending on the polarization rotation configuration employed. In the first case, the signal is rotated by an angle $\alpha_s < 90°$, so that a $\sin^2 \alpha_s$ fraction of the OPO signal flux density is coupled to the SHG fundamental a_4, while the remaining $\cos^2 \alpha_s$ fraction becomes the input signal a_2. For this configuration, we assume that the residual fundamental at the crystal output $a_4(l)$ is either coupled out of the cavity with a polarizing beamsplitter or strongly depleted, so that interference due to polarization mixing at the half-wave retarder is avoided.

In this configuration, the total resonator reflectance becomes $R_L \cos^2 \alpha_s$. There is no nonlinear output coupling in this situation; the intracavity signal flux density is not affected by the presence of the SHG process. Even though the SHG process is internal to the OPO resonator, this configuration is not different from external frequency doubling of a regular OPO. Since the SHG process does not benefit from high values of the intracavity signal flux density, this configuration is not expected to be particularly efficient.

If the residual fundamental $a_4(l)$ is not coupled out and α_s is set to 90°, the retarder switches around the polarizations of the OPO signal $a_2(l)$ and the residual fundamental $a_4(l)$ with no resulting interference due to polarization mixing. The OPO signal at the crystal output provides the SHG fundamental $a_4(0)$ for the next round trip, whereas the residual fundamental becomes the OPA input $a_2(0)$. Since the two processes are not coupled in the crystal, this configuration is conceptually equivalent to intracavity frequency doubling of a regular OPO with a second crystal. The plane-wave theory of such two-crystal intracavity-doubled OPO's has been presented elsewhere previously [18].
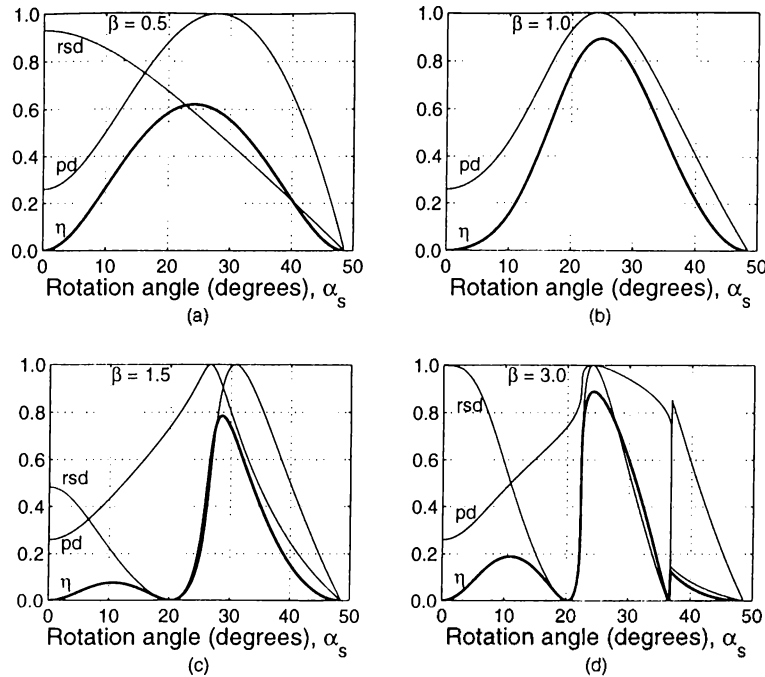
Figure 5.10: Conversion efficiency (η), pump depletion (pd), and rotated signal depletion (rsd) of class-C SD-OPO's as functions of the signal polarization rotation angle α_s for four different values of β. The nonlinear drive is kept constant at unity and $L = 0.04$ for (a) $\beta = 0.5$, (b) $\beta = 1.0$, (c) $\beta = 1.5$, and (d) $\beta = 3.0$.

5.2.3 Class-C SD-OPO's

In class-C SD-OPO's, the signal polarization rotation angle α_s can be adjusted to change the degree of coupling between the OPA and the SHG processes for a fixed value of β. Figure 5.10 shows the conversion efficiency and the depletion of the pump and the rotated signal as functions of α_s for four different values of β, where the nonlinear drive is kept constant at unity and $L = 0.04$. For $\beta = 0.5$ in Figure 5.10(a), a maximum conversion efficiency of 0.62 is achieved at $\alpha_s = 24°$, whereas the pump is fully depleted at $\alpha_s = 28°$. The depletion of the rotated signal starts at 0.93 with α_s just above zero and decreases monotonically until the SD-OPO gets below threshold at $\alpha_s = 49°$.

For $\beta = 1$ in Figure 5.10(b), the maximum conversion efficiency is higher (0.89) and complete pump depletion coincides with maximum conversion. For this particular value of β, the depletion of the pump and the rotated signal fields are equal for all values of α_s and D, similar to class-C SF-OPO's. However, simultaneous depletion of the pump and the rotated signal is possible only if β or $1/\beta$ is an odd integer.

For $\beta = 1.5$ and 3.0, the conversion efficiency curve has more than one peak

54

and the maximum conversion efficiency is 0.79 and 0.89, respectively. The intra-cavity signal flux density and consequently the conversion efficiency and depletion curves show discontinuities in their α_s dependence in Figure 5.10(d). In this case, the smallest solution of Equation (5.1) below $\alpha_s = 37°$ no longer satisfies Equation (5.1) as α_s is increased above 37°. If α_s varied up and down, a hysteresis behavior can be observed in the intracavity signal flux.

Figure 5.11 shows the conversion efficiency and the depletion of the pump and the rotated signal as functions of the nonlinear drive for four different values of β. In each case, α_s is adjusted to maximize the conversion efficiency at unity nonlinear drive. Maximum conversion occurs at a nonlinear drive close to unity for $\beta = 0.5$ and 1.5 and at exactly unity nonlinear drive for $\beta = 1.0$ and 3.0. However, the conversion efficiency drops from its maximum relatively quickly as the nonlinear drive is changed, when compared to class-A SD-OPO's (see Figure 5.9). This sensitivity to the nonlinear drive increases with increasing β.
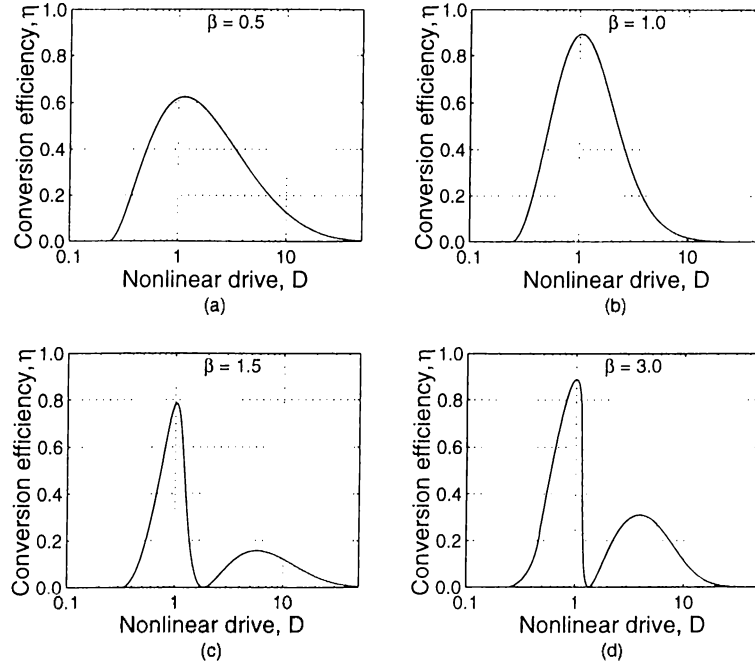
Figure 5.11: Conversion efficiency as a function of the nonlinear drive for four different values of β for a class-C SD-OPO. For each β value, the signal polarization rotation angle α_s is adjusted to maximize the conversion efficiency at $D = 1$. (a) $\beta = 0.5$, $\alpha_s = 24.1°$; (b) $\beta = 1.0$, $\alpha_s = 24.8°$; (c) $\beta = 1.5$, $\alpha_s = 28.8°$; (d) $\beta = 3.0$ $\alpha_s = 24.2°$. For each case, $L = 0.04$

Chapter 6

A Pulsed Plane-Wave Model

Even though the plane-wave theory of single-crystal upconversion OPO's presented in Chapters 4 and 5 describes the fundamental principles of these devices, it is inadequate for accurate modeling of practical experiments. Such a model requires one to include the effects of many experimental realities such as the temporal and transverse profiles of the fields, GVM, GVD, and self-phase modulation. As a first step, we found that developing a plane-wave model that takes into account the temporal profiles of the fields and the GVM between the pulses gives the most insight. This model does not take into account the Gaussian beam nature of the fields, chirped pulses, or group velocity dispersion.

In order to be able to compare the results of this pulsed plane-wave model with an actual experiment we decided to concentrate on class-C SF-OPO's [42], [9], [43]. In a pulsed class-C SF-OPO, the OPO pump and the rotated pump (higher frequency SFG input) get separated from each other as they propagate inside the crystal, since they have different group velocities. Since the signal gain is provided by the OPO pump, the intracavity signal pulse is approximately synchronized with this pump component and falls out of synchronization with the rotated pump. This reduces the efficiency of the SFG process. It was experimentally demonstrated that introducing a group delay between the orthogonally polarized pump components to compensate for the GVM inside the crystal maximizes the conversion efficiency [42].

Effects of pulse propagation can be incorporated into the plane-wave model by including time derivatives in the coupled mode equations. For class-C SF-OPO's Equations (3.5)-(3.9) become

$$\frac{\partial a_1}{\partial z} + \frac{1}{v_1} \frac{\partial a_1}{\partial t} = \kappa_a a_3 a_2 \qquad (6.1)$$

$$\frac{\partial a_2}{\partial z} + \frac{1}{v_2}\frac{\partial a_2}{\partial t} = \kappa_a a_3 a_1 - \kappa_b a_6 a_5 \qquad (6.2)$$

$$\frac{\partial a_3}{\partial z} + \frac{1}{v_3}\frac{\partial a_3}{\partial t} = -\kappa_a a_1 a_2 \qquad (6.3)$$

$$\frac{\partial a_5}{\partial z} + \frac{1}{v_5}\frac{\partial a_5}{\partial t} = -\kappa_b a_6 a_2 \qquad (6.4)$$

$$\frac{\partial a_6}{\partial z} + \frac{1}{v_6}\frac{\partial a_6}{\partial t} = \kappa_b a_2 a_5 \qquad (6.5)$$

where v_m are the group velocities for each field.

We used finite differencing techniques to compute numerical solutions of Equations (6.1)–(6.5) [41]. The values of the physical parameters used in our calculations are based on the experiment by Köprülü et $al.$ [42] and are summarized in Table 6.1. The refractive indices and group velocities are calculated using the dispersion relations for the nonlinear crystal KTP [44]. The dispersion in the

Physical parameter	Symbol	Value
Wavelengths (nm)	λ_1	2755.7
	λ_2	1182.4
	λ_3	827.4
	λ_5	827.4
	λ_6	486.8
Refractive indices	n_1	1.7870
	n_2	1.7448
	n_3	1.7575
	n_5	1.8419
	n_6	1.8019
Group velocities ($\times 10^8$ m/s)	v_1	1.6094
	v_2	1.6896
	v_3	1.6631
	v_5	1.5763
	v_6	1.5352
Effective nonlinear coefficients (pm/V)		
	d_e (OPO)	1.76
	d_e (SFG)	2.07
Total cavity reflectance	R_L	0.94
Crystal length (mm)	l	5

Table 6.1: Values of the physical parameters used in the pulsed plane-wave model calculations.

effective nonlinear coefficient is accounted for using Miller's Rule [38]. For conversion from average power to temporal profiles of field amplitudes, the beams are assumed to have uniform transverse profiles over a circular region of $28.8 \mu m$ diameter, the full-width at half-maximum (FWHM) diameter of the pump beam at the crystal focus [42]. The Ti:Sapphire pump laser used in the experiment has a repetition rate of 76 MHz. The pump pulse is modeled with a sech pulse shape that has an intensity FWHM of 170 fs.

We start out with a small signal pulse that has the same sech shape as the pump to represent the parametric fluorescence that the cavity oscillations build up from. This signal pulse is iterated through the cavity several times until a steady-state is reached. At each round trip, the signal pulse meets a new pump pulse and a fixed delay is introduced to the signal pulse in order to model the adjustment of the cavity length to synchronize the signal pulse with the OPO pump. The group delay between the OPO pump (a_3) and the rotated pump (a_5) at the input is also adjustable.

We compute the photon conversion efficiency for a series of cavity length (signal delay) values while keeping the polarization rotation angle α_p and group delay constant. We found that for a relevant range of α_p and group delay values, the signal delay required to maximize the conversion efficiency is in the 380–480 fs range. This is in agreement with the 472 fs group delay between the OPO pump and the signal in 5 mm of KTP. The maximum conversion efficiency obtained by varying the cavity length is taken to be the conversion efficiency at this α_p and group delay.

Next, we set the group delay between the pump components to 2 ps and calculated the conversion efficiency for different values of α_p. Figure 6.1 shows the results of this calculation for an average pump power of 515 mW together with experimental data points. We have made no attempts to fit the predictions of the model to the data by adjusting one of the physical parameters. The qualitative agreement of our model with the experimental results is very satisfactory. The quantitative agreement for the peak conversion efficiency, the optimum α_p, and the threshold α_p are reasonably good.

At zero group delay, we calculated the maximum conversion efficiency to be 22% at a polarization rotation angle of $\alpha_p = 30°$. These results are also in reasonable agreement with the 15% maximum conversion efficiency measured at $\alpha_p = 33°$ in the experiment.
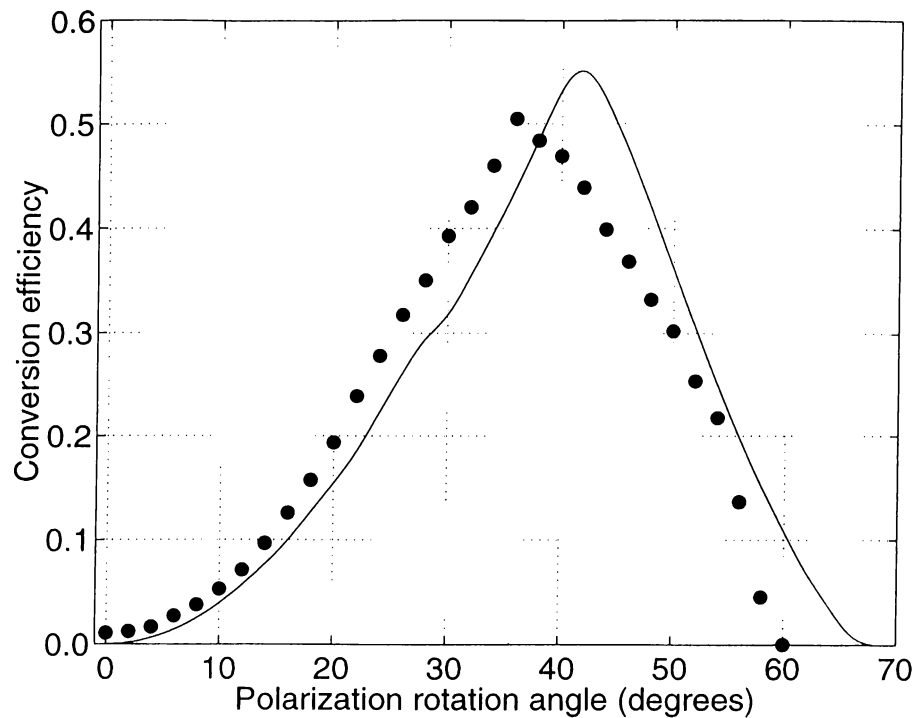
Figure 6.1: Conversion efficiency as a function of the pump polarization rotation angle α_p. The solid line represents the model's predictions and the filled circles correspond to experimental measurements. The average pump power is kept constant at 515 mW and the group delay between orthogonal pump components is 2 ps.

Our model predicted a pulse width of 210 fs for the sum-frequency output. This is also in good agreement with the 225 fs value measured in the experiment. Since our model does not take GVD into account, this agreement suggests that GVM is the dominating factor in determining the sum-frequency pulse width.

Chapter 7

Conclusions

The simultaneous phase matching of two different second-order nonlinear interactions within the same crystal with one or more fields in common leads to a wide range of frequency conversion applications. Both birefringent and quasi-phase matching techniques can be used to phase match the two interactions. Quasi-phase matching offers added flexibility in the choice of wavelengths, and brings adjustability to the relative strength of the two processes.

In this thesis, upconversion OPO's based on the simultaneous phase matching of OPO and SFG/SHG were investigated. We have identified four classes of SF-OPO's and three classes of SD-OPO's, depending on which field components are common. These seven classes of single-crystal upconversion OPO's are characterized by different sets of coupled mode equations, and consequently show different characteristics from each other. However, efficient upconversion is possible in all seven classes.

The most important design parameters for upconversion OPO's are the nonlinear drive and β. For a desired set of wavelengths, the nonlinear drive depends on the effective nonlinear coefficient d_e of the OPO process, the crystal length l, and the available pump photon flux density a_p^2. Even though the pump flux density can be adjusted by changing the beam size, experimental constraints may limit the maximum available a_p^2. The useful crystal length is also limited; physical limitations arise from crystal growth constraints, or in pulsed systems the pulse overlap length may be limited due to GVM between the field components. As a result, there is usually an upper limit to the available nonlinear drive. The parameter β is even more difficult to tailor. Once the phase matched wavelengths are known, BPM offers no method for adjusting β. However, using QPM for the

two processes provides a mechanism for adjusting β.

The remaining parameters that play an important role in the performance of single-crystal upconversion OPO's are the polarization rotation angle α and the cavity losses L. The polarization rotation required in five of the seven up-conversion OPO classes provides an adjustable parameter, α, that may easily be changed by rotating the half-wave retarder to maximize the conversion efficiency. The cavity losses are best minimized in all classes except class-A SF-OPO's; in a typical experiment one can usually keep $L < 0.05$. For class-A SF-OPO's how-ever, one of the cavity mirrors may have to be replaced with an output coupler for the signal field in order to maximize the conversion efficiency.

The practical design and optimization of single-crystal upconversion OPO's would benefit from the development of accurate computational models that take into account the transverse and temporal profiles of the fields, and other im-portant effects such as GVM, GVD, and self-phase modulation. As a first step toward this goal, we have extended the plane-wave theory of Chapters 4 and 5 to include the effects of temporal profiles of the fields and GVM. The results of this pulsed plane-wave model for a class-C SF-OPO are in good qualitative agreement with experimental measurements. The results also show that compensating for the GVM between orthogonal pump components of a class-C SF-OPO increases conversion efficiency considerably.

There are two main future directions for our work. The first is to incorpo-rate other experimental effects in the pulsed-plane wave model of Chapter 6, for predicting the performance of single-crystal upconversion OPO's more accu-rately. The incorporation of GVD and self-phase modulation requires one to add new terms to Equations (6.1)–(6.5). The incorporation of transverse profiles will increase the number of physical dimensions in Equations (6.1)–(6.5), and will therefore increase the computation time and memory requirements significantly.

The second future direction is to consider other combinations of second-order nonlinear interactions for different frequency conversion applications. The plane-wave theory of cascaded OPO's was recently investigated [45]. Another possibility is intracavity DFG of the signal and the idler of an OPO with a second nonlinear crystal, to provide long-wavelength radiation [46]. The generation of such long-wavelength radiation with a regular OPO may not be feasible because of phase matching limitations of available crystals [46]. The same combination can also be realized with simultaneous phase matching within the same nonlinear crystal.

References

[1] T. J. Driscoll, G. M. Gale, and F. Hache "Ti:sapphire 2nd-harmonic-pumped visible range femtosecond optical parametric oscillator," *Optics Communications*, vol. 110, pp. 638–644, 1994.

[2] G. M. Gale, M. Cavallari, and F. Hache "Femtosecond visible optical parametric oscillator," *Journal of the Optical Society of America B*, vol. 15, pp. 702–714, 1998.

[3] A. Nebel, H. Frost, R. Beigang, and R. Wallenstein "Visible femtosecond pulses by second harmonic generation of a cw mode-locked KTP optical parametric oscillator," *Applied Physics B*, vol. 60, pp. 453–458, 1995.

[4] R. J. Ellingson and C. L.Tang "High-power, high-repetition-rate femtosecond pulses tunable in the visible," *Optics Letters*, vol. 18, pp. 438–440, 1993.

[5] D. T. Reid, M. Ebrahimzadeh, and W. Sibbett "Efficient femtosecond pulse generation in the visible in a frequency-doubled optical parametric oscillator based on RbTiOAsO$_4$," *Journal of the Optical Society of America B*, vol. 12, pp. 1157–1163, 1995.

[6] E. C. Cheung, K. Koch, and G. T. Moore "Frequency upconversion by phase-matched sum-frequency generation in an optical parametric oscillator." *Optics Letters*, vol. 19, pp. 1967–1969, 1994.

[7] A. Shirakawa, H. W. Mao, and T. Kobayashi "Highly efficient generation of blue-orange femtosecond pulses from intracavity-frequency-mixed optical parametric oscillator," *Optics Communications*, vol. 123, pp. 121–128, 1996.

[8] T. Kartaloğlu, K. G. Köprülü, and O. Aytür "Phase-matched self-doubling optical parametric oscillator," *Optics Letters*, vol. 22, pp. 280–282, 1997.

[9] K. G. Köprülü, T. Kartaloğlu, and O. Aytür "Single-crystal sum-frequency generating optical parametric oscillator," in *Conference on Lasers and Electro-Optics*, volume 11 of *OSA Technical Digest Series*, pp. 457–458, Washington, D.C., 1997. Optical Society of America.

[10] P. P. Bey and C. L. Tang "Plane-wave theory of parametric oscillator and coupled oscillator-upconverter," *IEEE Journal of Quantum Electronics*, vol. 8, pp. 361–369, 1972.

[11] J. E. Bjorkholm "Some effects of spatially nonuniform pumping in pulsed optical parametric oscillators," *IEEE Journal of Quantum Electronics*, vol. 7, pp. 109–118, 1971.

[12] A. V. Smith, W. J. Alford, T. D. Raymond, and M. S. Bowers "Comparison of a numerical model with measured performance of a seeded, nanosecond KTP optical parametric oscillator," *Journal of the Optical Society of America B*, vol. 12, pp. 2253–2267, 1995.

[13] M. F. Becker, D. J. Kuizenga, D. W. Phillion, and A. E. Siegman "Analytic expressions for ultrashort pulse generation in mode-locked optical parametric oscillators," *Journal of Applied Physics*, vol. 45, pp. 3996–4005, 1974.

[14] E. C. Cheung and J. M. Liu "Theory of a synchronously pumped optical parametric oscillator in steady-state operation," *Journal of the Optical Society of America B*, vol. 7, pp. 1385–1401, 1990.

[15] E. C. Cheung and J. M. Liu "Efficient generation of ultrashort, wavelength-tunable infrared pulses," *Journal of the Optical Society of America B*, vol. 8, pp. 1491–1506, 1991.

[16] J. M. Liu, G. Zhou, and S. J. Pyo "Parametric gain of the generation and the amplification of ultrashort optical pulses," *Journal of the Optical Society of America B*, vol. 12, pp. 2274–2287, 1995.

[17] G. T. Moore and K. Koch "Optical parametric oscillation with intracavity sum-frequency generation," *IEEE Journal of Quantum Electronics*, vol. 29, pp. 961–969, 1993.

[18] G. T. Moore, K. Koch, and E. C. Cheung "Optical parametric oscillation with intracavity second-harmonic generation," *Optics Communications*, vol. 113, pp. 463–470, 1995.

[19] R. W. Boyd. *Nonlinear Optics*. Academic Press, San Diego, 1992.

[20] B. E. A. Saleh and M. C. Teich. *Fundamentals of Photonics*. Wiley-Interscience, New York, 1991.

[21] R. A. Baumgartner and R. L. Byer "Optical parametric amplification," *IEEE Journal of Quantum Electronics*, vol. 15, pp. 432–444, 1979.

[22] S. E. Harris "Tunable optical parametric oscillators," *Proceedings of the IEEE*, vol. 57, pp. 2096–2113, 1969.

[23] C. L. Tang and L. K. Cheng. *Fundamentals of Optical Parametric Processes and Oscillators*. Harwood Academic, Amsterdam, 1995.

[24] L. E. Myers, R. C. Eckardt, M. M. Fejer, R. L. Byer, W. R. Bosenberg, and J. W. Pierce "Quasi-phase-matched optical parametric oscillators in bulk periodically poled LiNbO$_3$," *Journal of the Optical Society of America B*, vol. 12, pp. 2102–2116, 1995.

[25] M. M. Fejer, G. A. Magel, D. H. Jundt, and R. L. Byer "Quasi-phase-matched second harmonic generation: tuning and tolerances," *IEEE Journal of Quantum Electronics*, vol. 28, pp. 2631–2654, 1992.

[26] M. Abramowitz and I. A. Stegun, eds. *Handbook of Mathematical Functions with Formulas, Graphs, and Mathematical Tables*. Dover, New York, 1965.

[27] R. L. Byer and S. E. Harris "Power and bandwidth of spontaneous parametric emission," *Physical Review*, vol. 168, pp. 1064–1068, 1968.

[28] R. L. Burden and J. D. Faires. *Numerical Analysis*. PWS Publishing Company, Boston, fifth edition, 1993.

[29] O. Aytür and Y. Dikmelik "Plane-wave theory of self-doubling optical parametric oscillators," *IEEE Journal of Quantum Electronics*, vol. 34, pp. 447–458, 1998.

[30] Y. Dikmelik, G. Akgün, and O. Aytür "Plane-wave dynamics of optical parametric oscillation with simultaneous sum-frequency generation," submitted for publication in *IEEE Journal of Quantum Electronics*, July 1998.

[31] C. McGowan, D. T. Reid, Z. E. Penman, M. Ebrahimzadeh, W. Sibbett, and D. H. Jundt "Femtosecond optical parametric oscillator based on periodically poled lithium niobate," *Journal of the Optical Society of America B*, vol. 15, pp. 694–701, 1998.

[32] D. T. Reid, G. T. Kennedy, A. Miller, W. Sibbett, and M. Ebrahimzadeh "Widely tunable, near- to mid-infrared femtosecond and picosecond optical parametric oscillators using periodically poled LiNbO$_3$ and RbTiOAsO$_4$," *IEEE Journal of Selected Topics in Quantum Electronics*, vol. 4, pp. 238–248, 1998.

[33] S. D. Butterworth, P. G. R. Smith, and D. C. Hanna "Picosecond Ti:Sapphire-pumped optical parametric oscillator based on periodically poled LiNbO$_3$," *Optics Letters*, vol. 22, pp. 618–620, 1997.

[34] M. Vaidyanathan, R. C. Eckardt, V. Dominic, L. E. Myers, and T. P. Grayson "Cascaded optical parametric oscillations," *Optics Express*, vol. 1, pp. 49–53, 1997.

[35] V. Petrov and F. Noack "Frequency upconversion of tunable femtosecond pulses by parametric amplification and sum-frequency generation in a single nonlinear crystal," *Optics Letters*, vol. 20, pp. 2171–2173, 1995.

[36] R. A. Andrews, H. Rabin, and C. L. Tang "Coupled parametric downconversion and upconversion with simultaneous phase matching," *Physical Review Letters*, vol. 25, pp. 605–608, 1970.

[37] O. Pfister, J. S. Wells, L. Hollberg, L. Zink, D. A. Van Baak, M. D. Levenson, and W. R. Bosenberg "Continuous-wave frequency tripling and quadrupling by simultaneous three-wave mixings in periodically poled crystals: application to a two-step 1.19–10.71-μm frequency bridge," *Optics Letters*, vol. 22, pp. 1211–1213, 1997.

[38] D. A. Roberts "Simplified characterization of uniaxial and biaxial nonlinear optical crystals," *IEEE Journal of Quantum Electronics*, vol. 28, pp. 2057–2074, 1992.

[39] W. R. Bosenberg, J. I. Alexander, L. E. Myers, and R. W. Wallace "2.5-W, continuous-wave, 629-nm solid-state laser source," *Optics Letters*, vol. 23, pp. 207–209, 1998.

[40] G. Akgün, Y. Dikmelik, and O. Aytür "Plane-wave dynamics of optical parametric oscillation with simultaneous sum-frequency generation," in *Nonlinear Optics: Materials, Fundamentals, and Applications Topical Meeting*, Hawaii, August 1998. Optical Society of America.

[41] W. H. Press, S. A. Teukolsky, W. T. Vetterling, and B. P. Flannery. *Numerical Recipes in C*. Cambridge Univ., Cambridge, second edition, 1992.

[42] K. G. Köprülü, T. Kartaloğlu, Y. Dikmelik, and O. Aytür "Single-crystal sum-frequency generating optical parametric oscillator," submitted for publication in *Journal of the Optical Society of America B*, August 1998.

[43] K. G. Köprülü, T. Kartaloğlu, Y. Dikmelik, and O. Aytür "Advances in femtosecond single-crystal sum-frequency generating optical parametric oscillators," in *Nonlinear Optics: Materials, Fundamentals, and Applications Topical Meeting*, Hawaii, August 1998. Optical Society of America.

[44] K. Kato "Parametric oscillation at 3.2 μm in KTP pumped at 1.064 μm," *IEEE Journal of Quantum Electronics*, vol. 27, pp. 1137–1140, 1991.

[45] G. T. Moore, K. Koch, M. E. Dearborn, and M. Vaidyanathan "A simultaneously phase-matched tandem optical parametric oscillator," *IEEE Journal of Quantum Electronics*, vol. 34, pp. 803–810, 1998.

[46] K. Koch, G. T. Moore, and E. C. Cheung "Optical parametric oscillation with intracavity difference-frequency mixing," *Journal of the Optical Society of America B*, vol. 12, pp. 2268–2273, 1995.